INFORMATION TO USERS

This manuscript has been reproduced from the microfilm master. UMI films the text directly from the original or copy submitted. Thus, some thesis and dissertation copies are in typewriter face, while others may be from any type of computer printer.

The quality of this reproduction is dependent upon the quality of the copy submitted. Broken or indistinct print, colored or poor quality illustrations and photographs, print bleedthrough, substandard margins, and improper alignment can adversely affect reproduction.

In the unlikely event that the author did not send UMI a complete manuscript and there are missing pages, these will be noted. Also, if unauthorized copyright material had to be removed, a note will indicate the deletion.

Oversize materials (e.g., maps, drawings, charts) are reproduced by sectioning the original, beginning at the upper left-hand corner and continuing from left to right in equal sections with small overlaps. Each original is also photographed in one exposure and is included in reduced form at the back of the book.

Photographs included in the original manuscript have been reproduced xerographically in this copy. Higher quality 6" x 9" black and white photographic prints are available for any photographs or illustrations appearing in this copy for an additional charge. Contact UMI directly to order.

UMI

A Bell & Howell Information Company
300 North Zeeb Road, Ann Arbor MI 48106-1346 USA
313/761-4700 800/521-0600

QUASIPARTICLE BOUND STATES IN NORMAL METAL / SUPERCONDUCTOR STRUCTURES PROBED BY SCANNING TUNNELING MICROSCOPY

BY

STUART HOLDEN TESSMER

B.S., University of Washington, 1989
M.S., University of Illinois, 1992

THESIS

Submitted in partial fulfillment of the requirements
for the degree of Doctor of Philosophy in Physics
in the Graduate College of the
University of Illinois at Urbana-Champaign, 1995

Urbana, Illinois

UMI Number: 9624511

UMI Microform 9624511
Copyright 1996, by UMI Company. All rights reserved.

This microform edition is protected against unauthorized
copying under Title 17, United States Code.

UMI
300 North Zeeb Road
Ann Arbor, MI 48103

UNIVERSITY OF ILLINOIS AT URBANA-CHAMPAIGN

THE GRADUATE COLLEGE

JULY 1995

WE HEREBY RECOMMEND THAT THE THESIS BY

STUART HOLDEN TESSMER

ENTITLED QUASIPARTICLE BOUND STATES IN NORMAL METAL / SUPERCONDUCTOR STRUCTURES PROBED BY SCANNING TUNNELING MICROSCOPY

BE ACCEPTED IN PARTIAL FULFILLMENT OF THE REQUIREMENTS FOR

THE DEGREE OF DOCTOR OF PHILOSOPHY

Dale J. Van Harlingen
Director of Thesis Research

Head of Department

Committee on Final Examination†

Dale J. Van Harlingen
Chairperson

W. P. Wiesman

Steven Errede

Paul M. Goldbart

† Required for doctor's degree but not for master's.

O-517

© Copyright by Stuart Holden Tessmer, 1995

QUASIPARTICLE BOUND STATES
IN NORMAL METAL / SUPERCONDUCTOR STRUCTURES
PROBED BY SCANNING TUNNELING MICROSCOPY

Stuart Holden Tessmer
Department of Physics
University of Illinois at Urbana-Champaign, 1995
Dale J. Van Harlingen, Advisor

In this work we consider systems in which small normal-metal structures (N) are put into contact with a large superconductor (S), with the goal of spatially characterizing the superconductivity. Confined regions with suppressed superconductivity will support quasiparticle bound states, which can be measured spectroscopically. Using a custom-built cryogenic scanning tunneling microscopy system, we have probed the bound states of an NS system consisting of Au (N) droplets of nanometer dimensions in electrical contact with bulk $NbSe_2$ (S). A quasiparticle bound state was observed even when tunneling directly into the $NbSe_2$, clear evidence for a significant reduction of the superconductivity inside the $NbSe_2$ induced by the proximity of the Au over-layer. By invoking a proximity effect model, we are able to characterize the vertical and lateral variation of the pair potential Δ inside the superconductor. We find that a severe suppression occurs which is beyond the conventional theory. We believe that this effect arises from the short coherence length of the superconductor, so that the spatial variation of the interaction parameter g becomes important. The profile of Δ that we extract from our data then combines both the conventional proximity suppression of Δ and its modulation by the profile of g, representing the first observation of spatial structure of the interaction parameter.

This thesis is dedicated to

Forrest Leonard Tessmer.

ACKNOWLEDGMENTS

The completion of this work would not have been possible without the considerable support and assistance I received from many people. Without doubt, the most fortunate turn of events in my academic career was getting the chance to work with Professor Dale J. Van Harlingen. He has been an outstanding thesis advisor in every way, teaching a wealth of physics, showing great patience and support, while giving me more respect than I deserved. Not surprisingly, I have also come to consider him as a good friend. In addition, I am in debt to Professors Joseph W. Lyding and Paul M. Goldbart for lending a considerable amount of assistance and expertise to this research. For contributing to this research by giving me advice on numerous occasions, and for all their support in general, I thank Professors Laura H. Greene and James P. Wolfe.

With regard to interpreting and understanding experimental results, I have been very lucky to work with outstanding theorists. Martin Tarlie has generously devoted countless hours to this work and deserves a great deal of credit for its success. To this end, I thank Dmitrii Maslov for helping me to understand the underlying physics of this research, and for his insightful contribution to the analysis of the data. I have also learned a good deal of physics thanks to discussions with Branko Stojkovic, Professor John R. Tucker, and Nir Hass. My fellow group members, Britton Plourde, Ralph Schweinfurth, Subashri Rao, Mark Wistrom, Dave Wollman, Brian Yanoff, Joe Walko, Lan Vu, and Fred Sharifi have helped in ways too numerous to list. For all their help in making our scanning tunneling microscopy system work, I thank Gordan Gammie, Jerome Hubecek, T.-C. Shen, Steve Skala, and Ting Chen.

Much of this work would have been a great deal more difficult without the friendly and knowledgeable help of the MRL support staff, especially Carroll Sarver, Bud Dittman, Alex Greene, and Judy Baker. I also thank all the people I've become friends

with on the basketball court and soccer field. Although they didn't contribute directly to this work, they've certainly helped me maintain my sanity and well-being.

Finally, I would like to thank my family, Ilsa, Maurice, Dave, Vicky, and Roxanne for their endless support and encouragement. I especially express appreciation for my wife, Antoinette. She has made countless sacrifices in the unselfish support of my career.

This work has been supported by the National Science Foundation under Materials Research Laboratory Grant No. NSF-DMR89-20538, and a grant from the Research Board of the University of Illinois. I have also received support from the Physics Department Summer Fellowship during my first year, and the GAANN Fellowship in Physics during my last year of graduate school.

TABLE OF CONTENTS

1. INTRODUCTION

Soon after experimentally demonstrating the first local and variable vacuum tunneling barrier in 1981, Binnig and Rohrer developed the scanning tunneling microscope (STM) which brought about a new era of surface science.[1] Electron tunneling was known for many years, ever since the formulation of quantum mechanics. But prior to 1981, a vacuum tunneling barrier was considered unattainable experimentally. The problem was that to achieve a detectable current a vacuum gap of only ~10 Å would need to be established and maintained. Moreover, due to the exponential dependence of the signal, vibrations ~0.1 Å would need to be eliminated. For this reason, electron tunneling had been experimentally realized only by using material insulating barriers, such as a thin oxide layer. For example, Giaever's pioneering electron-tunneling spectroscopy experiments relied on an oxide barrier to tunnel into superconducting Pb.[2]

The construction of an STM is very simple in principle. The basic requirement is the capability to control the position of a sharp metallic tip in close proximity to a conductive sample, while monitoring the tunnel current. Binnig and Rohrer overcame the problem of the small gap size by bringing the tip into position with high-resolution piezoelectric actuators, accurate to about 0.05 Å. In addition, great care was taken to ensure extraordinary mechanical stability and to isolate the STM from vibrations. The unprecedented resolution of the instrument was demonstrated dramatically by rastering the tip over a rectangular area of length 100 Å above the Si (111) surface.[3] Amazingly, by imaging individual Si atoms on the surface, the structure of the famous 7×7 reconstruction could be determined directly in real space. For their invention, Binnig and Rohrer were awarded the 1986 Nobel Prize in Physics.

The spatial resolution attainable with STM made studying the nanoscale characteristics of numerous systems possible for the first time. The subsequent development of cryogenic scanning tunneling microscopy (CSTM) permitted Giaever's techniques to be applied to the junction formed by the tip and a superconducting sample. This extended the imaging capabilities of STM to nanometer resolution electron-tunneling spectroscopy. In fact, experimenters have found that the STM can work well over a wide temperature range and in a variety of environments. STM has established itself as an invaluable tool in the fields of physics, engineering, chemistry, and biology.

The nanoscale spectroscopic capabilities of CSTM gives it great potential for the study of superconductivity. The first experimenters to exploit this potential successfully were Hess *et al.* who probed magnetic vortices in superconducting $NbSe_2$.[4] This experiment serves as an outstanding example of how powerful CSTM can be as a probe of superconductivity. The measurements showed a striking feature in the electronic density of states at the Fermi energy: a pronounced peak when the tip was positioned directly above the center of a vortex. Initially, this came as a great surprise to experimentalists and theorists alike. Prior to this experiment, the conventional wisdom assumed that CSTM spectroscopy would be similar to the standard Giaever measurements. However, there is a key difference: a planar tunnel junction probes the average behavior of many excitations over the area of the junction, while the local nature of STM tunneling allows for the possibility to observe individual electronic wavefunctions. Six months after the initial measurements, theorists showed that Hess' peak follows from the quantum mechanics of a superconducting vortex.[5] The physics is conceptually simple, much like the familiar problem of a particle-in-a-box. In a superconducting system, the electron-like single-particle excitations are known as quasiparticles. A vortex presents a region of reduced superconductivity forming a potential well for the quasiparticles. Near the Fermi energy, discrete quasiparticle bound states form inside the vortex. In analogy to the particle-in-a-box, the wavefunction of the

lowest energy bound state has the highest amplitude near the vortex center. Thus, there is a Fermi level peak in the density of states at this region.

Because the above explanation relies on theory that has been well established since the 1960's, it seems surprising that the spatial structure of quasiparticles bound in vortex was completely unanticipated. Perhaps this was justified prior to the invention of the STM when such small length scales were experimentally inaccessible. However, for at least a year prior to Hess' successful measurements, it was well known that experimenter were attempting to study vortices by CSTM. While many theorists understood the potential sensitivity to electronic structure, no one thought to explore the consequences of locally probing a region with bound wavefunctions. Indeed, by extending the reach of electronic measurements to atomic length scales, the STM has directed physicists to new and exciting phenomena.

This work addresses a superconducting system in which small normal metal particles (N) have been put into contact with a large superconductor (S). The superconductivity is reduced in the normal metal, forming a region electronically similar to a magnetic vortex, which supports quasiparticle bound states. Our focus is to apply CSTM as a probe of the variation of superconductivity due to the proximity of the normal metal. Before any measurements could be taken, a great deal of time and effort went into the design and construction of the CSTM system. Our apparatus is described in detail in Chapter 2. For use in comparison to the NS measurements, Chapter 3 shows a baseline of measurements of isolated superconductors. Chapter 4 then describes the basic theory of bound states in NS structures. Lastly, our observations and analysis of the Au (N)-$NbSe_2$ (S) system are presented in Chapters 5, 6, and 7.

2. CRYOGENIC SCANNING TUNNELING MICROSCOPY (CSTM)

2.1 Basic Principals of STM and CSTM

STM is based on the quantum mechanical phenomenon of electron tunneling. When two conductive materials are brought sufficiently close together, the wavefunctions of the conduction electrons overlap. This allows electrons to traverse the classically forbidden region between the two materials. A tunneling current I can be produced by the application of a bias voltage V between the two conductors, which gives a preferred tunneling direction. In addition to the voltage dependence, the current depends on the electronic density of states , the temperature T, and the separation σ of the two materials. An STM consists of two such electrodes: a sharp metallic tip, and a conductive sample. As the tunneling current falls off exponentially with σ, STM is an extremely sensitive measure of variations in tip-sample spacing. The lateral resolution is determined by the geometry of the tip which confines the current to a narrow channel. The width of the current channel can be as small as ~1 Å, orders of magnitude better than other local probes, such as point-contact spectroscopy.

The key innovation of scanning tunneling microscopy was to mount the tunneling probe on a three-dimensional piezoelectric drive, as shown in Figure 2.1. This allows the tip to be positioned at various locations x,y so that the sample's topography or electronic structure can be mapped out with atomic resolution. In terms of the electronic structure, there is a great advantage to operating an STM cryogenically: at sufficiently low T, the local density of states $N(E,x,y)$ can be directly measured on the sample surface with atomic resolution. Hence, CSTM represents the ultimate local probe of the electronic structure of a surface.

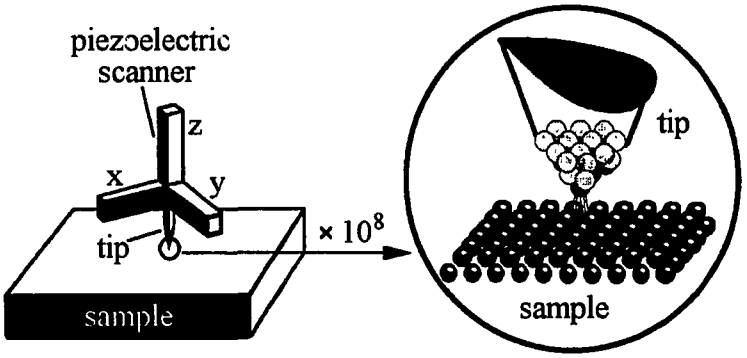

Fig. 2.1 (Left) Geometry of the Scanning Tunneling Microscope.[6] (Right) Atomic-scale enlargement of the tip and sample. The short lines indicate the path of the tunneling electrons.

2.1.1 Control of the STM tip

Piezoelectric ceramics provide direct electromechanical conversion, with conversion factors ranging typically from a few to several hundred angstroms per volt. Originally, the designs of most STMs consisted of a tripod of piezoelectric rods to provide the necessary *x, y,* and *z* motion for the tunneling tip (see Figure 2.1). The *x* and *y* rods rastered the tip over the surface of the sample, while the *z* rod controlled the tip/sample separation. More recent STMs, with improved vibrational tolerances, instead use piezoelectric tube-scanners which are more easily incorporated into compact and rigid designs. These tubes are fashioned into four quadrants that can each be made to lengthen or shorten independently. The *z* motion is accomplished simply by changing the length of the four quadrants in unison. To get *x* or *y* motion, one quadrant is lengthened while the opposing quadrant is shortened. Because the tip is coaxially mounted, the net *z* displacement is negligible, but there is lateral displacement as the tube bends in the direction of the shortened side. In this way, a single tube-scanner achieves the full three-dimensional motion necessary for the tunneling tip.

Figure 2.2 shows a schematic of our control electronics, which is based on typical designs.[7] We obtain the topography of the sample in the usual way, called the constant-current mode. Once the tip, electronically held at virtual ground, is brought into tunneling range, a current is established due to the bias voltage V applied to the sample. An amplifier of gain 10^8 V/A converts the signal into a voltage, which is compared to a reference voltage chosen to yield a desired tunneling current. The resulting error signal is fed into a circuit element which creates a feedback voltage. The feedback is a combination of a voltage proportional to the error, and a voltage proportional to the error's integral. If applied to the piezoelectric element controlling the *z*-position of the tip, the feedback maintains the tip/sample spacing consistent with the desired tunneling

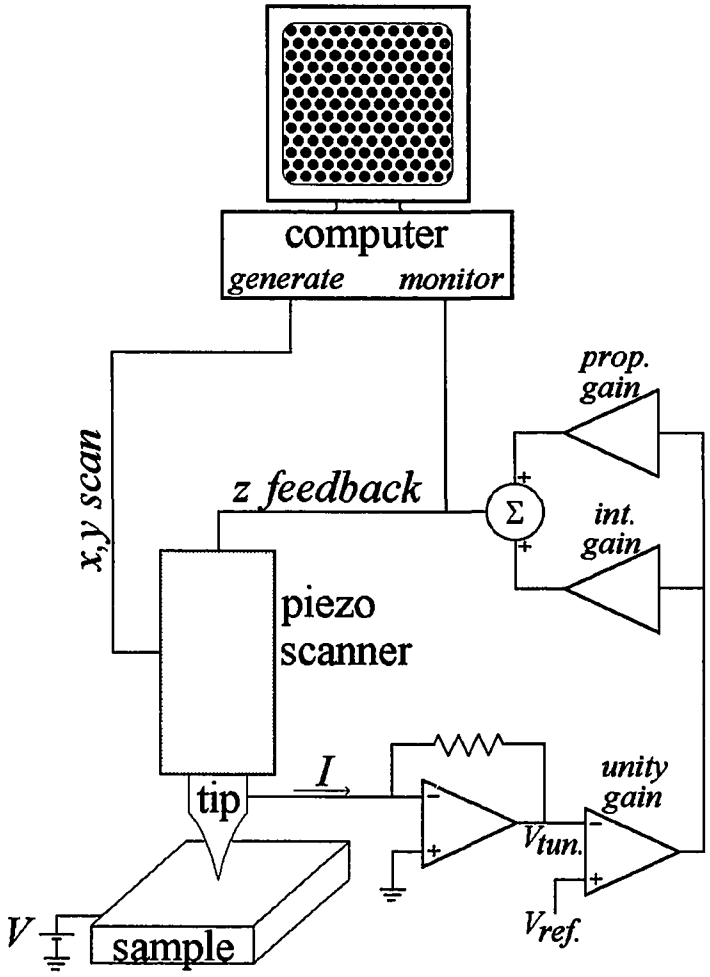

Fig. 2.2 Schematic of the electronic circuitry used to control the motion of the tip while generating a topographic image of the sample surface.

current. While the tip is moved in the x direction, the feedback necessary to keep a constant tunneling current can be monitored. Under the assumptions of a constant local work function and local density of states (at the particular V), the feedback signal represents a profile of constant tip-sample separation along this line. The full topographic image can then be constructed from multiple profiles obtained by rastering the tip over a rectangular area.

2.1.2 STM resolution

To better understand how the STM achieves its outstanding spatial resolution, we begin by examining the system with respect to z, parallel to the direction in which the tip points (this direction will also be perpendicular to the surface of the tip at the point closest to a planar sample surface). We can understand why the tunneling current falls off so abruptly with tip-sample separation σ by considering the basic quantum mechanics in one dimension. If the bias voltage is small compared to the work functions of the tip and sample, then to a good approximation the tunneling barrier can be taken to be rectangular with height equal to the average of the two work functions ϕ_{av}. We assume that the transmission coefficient across the barrier is much less than unity to further simplify the calculation. Now for an incident electron near the Fermi level in the sample, the wavefunction falls off inside the barrier as $\psi(z) = Ae^{-\kappa z}$, where $\kappa = \sqrt{2m\phi_{av}}/\hbar$, and A is roughly unity, as sketched in Figure 2.3. After traversing the barrier, the wavefunction resumes its oscillation as $\psi(z) = \mathcal{T} e^{ik_F z}$, where k_F is the Fermi wave number and $\mathcal{T}$ is the transmission coefficient. Because our assumptions imply $\kappa\sigma >> 1$, the wavefunction slope $d\psi/dz$ is approximately zero as the wavefunction approaches the vacuum/tip interface. The continuity of ψ and $d\psi/dz$ then requires that the value of the wavefunction at the interface be equal to its amplitude inside the tip, $\psi(\sigma) = Ae^{-\kappa\sigma} = |\mathcal{T}|$. That is to say, the absolute value of the transmission coefficient is exponential in σ. As the tunneling

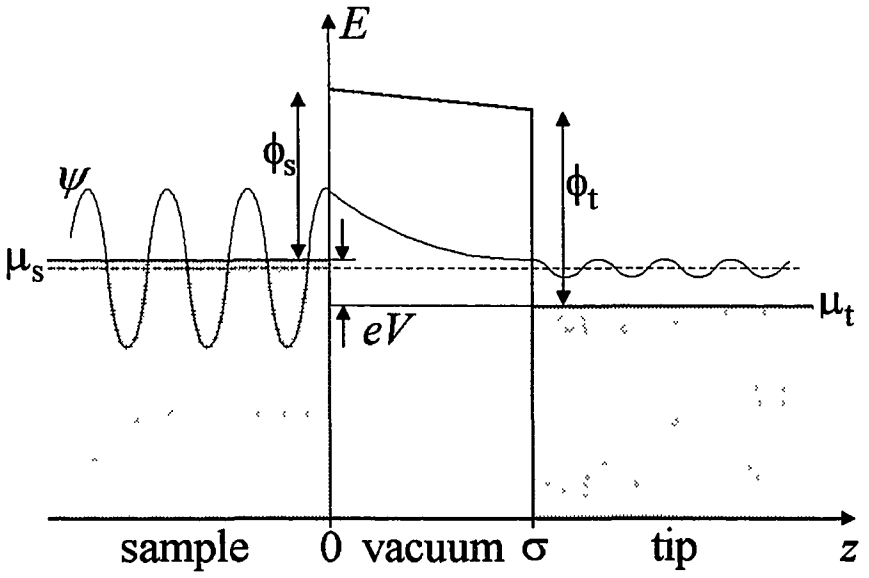

Fig. 2.3 The vacuum barrier as a function of z, shown with a tunneling electronic wavefunction ψ superimposed. The quantities $\mu_{s(t)}$ and $\phi_{s(t)}$ refer respectively to the chemical potential and work function of the sample (tip).

current is proportional to the transmission probability $|\mathcal{T}|^2$, we immediately confirm that it is also exponential in σ:

$$I \propto e^{-2\kappa\sigma}. \qquad 2.1$$

Calculations of far greater detail and precision have been performed considering such issues as tip sharpness and the effects of different atomic orbitals on the tip or sample. Although these factors affect the exact expression for the tunneling current, the z-dependence given by Eq. 2.1 remains approximately correct. Since typical work functions are about 3 eV, $\kappa \sim 1$ Å^{-1}. Hence, the tunneling current drops by nearly an order of magnitude for each additional 1 Å of tip-sample separation. As I can be measured to an accuracy of 1% in most cases, STMs routinely achieve a z resolution $\sim 10^{-12}$ m!

The exponential z sensitivity of the STM directly leads to its outstanding x-y resolution. This follows from the fact that tunneling tips usually have a small cluster of atoms, if not a single atom, which is closer to the surface than all the others. Even if the proximity difference is slight, a distance as small as a single angstrom will cause the majority of the tunneling to occur at this point. As indicated in Figure 2.1, an effective tunneling tip of atomic dimensions results, which in turn localizes the sampled area of the surface to atomic dimensions. Stoll *et al.* have examined STM tunneling in detail, solving for the incident and transmitted wavefunctions in three dimensions.[8] The resulting current density is shown in Figure 2.4, for which the following typical parameters were used: ϕ_{av}=2.41 eV, σ=4 Å, and a tip curvature radius of 1.7 Å. We see that most of the tunneling current is confined to a channel of radius 3 Å on the sample surface. This sets the x-y resolution for STM topographical and electronic measurements. In terms of topography, the sensitivity is sufficient to detect the corrugation of individual atoms, in agreement with countless experimental demonstrations.

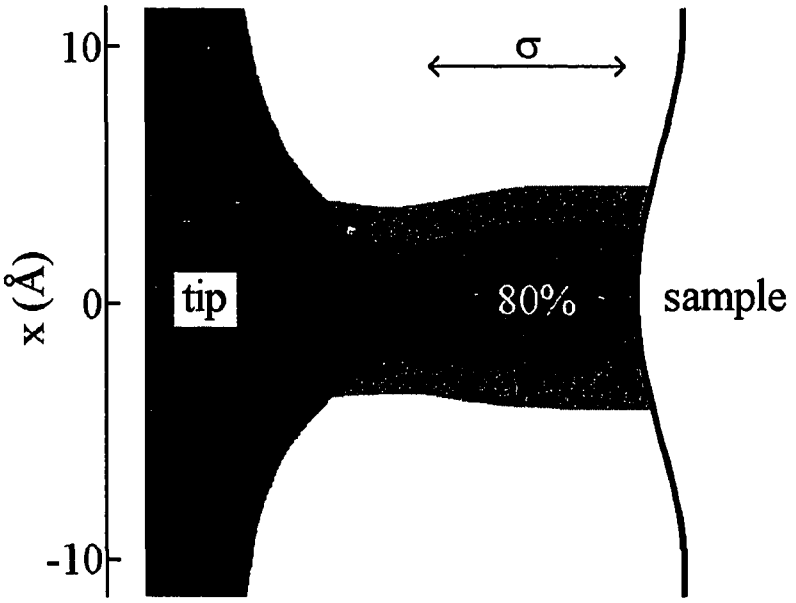

Fig. 2.4 Calculated current density distribution for tunneling from a tip to a corrugated surface, assuming an effective barrier height of 2.41 eV, a tip radius of 1.7 Å, and σ=4 Å.[8]

2.1.3 CSTM spectroscopy

The electronic structure of the sample can be obtained by interrupting the scanning and holding the position of the tip fixed. Now the voltage can be varied to get the local *I-V* characteristics. However at room temperature, thermal excitations in the tip and sample mask most of the electronic features, with only features ~1 eV discernible. The achievable energy resolution greatly improves by going to low temperatures, ~1 K. In addition, to observe superconducting phenomena, as is the focus of this work, the sample must be cooled to below the relevant transition temperature; hence, CSTM is essential. The following discussion quantitatively introduces the significance of CSTM *I-V* measurements.

To obtain an expression relating the tunneling current to the electronic structure of the tip (t) and sample (s), we begin with the usual assumption that tunneling transitions all occur at constant energy after adjusting the relative chemical potentials by eV to account for the applied bias voltage,[9] as indicated in Figure 2.3. The total current can then be calculated by summing up all the contributions from each energy level. At a given energy E, for temperatures $T>0$, the number of occupied states in the sample is $N_s(E)f(E)$ where N is the density of states of the electrode and f is the usual Fermi function $f(E)=1/(e^{E/k_BT}+1)$. Electrons in these states can tunnel only into empty states of the tip, the number of which is given by $N_t(E-eV)[1-f(E-eV)]$. The tunneling current from the sample to the tip can then be written as

$$I_{s\to t} \propto \int_{-\infty}^{\infty} |\mathcal{T}|^2 N_s(E) f(E) N_t(E-eV)\left[1-f(E-eV)\right]dE$$

where $|\mathcal{T}|^2$ is the transmission probability for tunneling from a particular initial to final state. This quantity is independent of E to a good approximation, if only energies close to the Fermi level are considered. To be more precise, if V and k_BT/e are much less than the tunneling potential barrier, typically ≈3 V for STM, then the $|\mathcal{T}|^2$ factor can be pulled out of the integral and absorbed into the constant of proportionality. The net tunneling current is obtained by subtraction of the reverse current $I_{t\to s}$. We find

$$I \propto \int_{-\infty}^{\infty} N_s(E) N_t(E-eV)[f(E)-f(E-eV)]dE.$$

To facilitate further simplifications, we make use of the fact that STM tips are typically composed of noble metals and alloys, such as Au or PtIr, which have a constant density of states near the Fermi level, i.e., N_t is independent of E. Differentiation with respect to eV then relates the differential conductance dI/dV to the density of states of the sample:

$$\frac{dI}{dV}(V) \propto \int_{-\infty}^{\infty} N_s(E)\left[-\frac{\partial f(E-eV)}{\partial(eV)}\right]dE. \qquad 2.2$$

Since $-\partial f(E-eV)/\partial(eV)$ is a bell-shaped weighting function peaked at $E=eV$, with width ~k_BT and unit area under the curve, it is clear that as $k_BT\to 0$, Eq. 2.2 approaches

$$\left.\frac{dI}{dV}(V)\right|_{T=0} \propto N_s(eV). \qquad 2.3$$

Thus, we see that in the low temperature limit, the differential conductance gives a direct measure of the sample's density of states. By performing this spectroscopic

measurement at arbitrary x,y tip positions, CSTM represents an unprecedented probe of electronic structure, yielding the complete local density of states of a surface, $N(E,x,y)$.

2.2 Integrated CSTM and Sample Preparation System

2.2.1 Design criteria

STM designs and techniques have undergone considerable improvements since the pioneering work of Binnig and Rohrer.[1,2] Instrumentation development has closely followed scientific progress, to meet the demands of numerous experiments in a variety of research fields. In our case, the goal was to construct a cryogenic STM system (CSTM) suitable for the study of superconducting systems with nanoscale structures. Before embarking on a full scale design, preliminary experiments were conducted to determine the most important design considerations. For this purpose, a modest system was constructed which consisted of an STM scanning head mounted on a 120 cm length of stainless-steel tubing. A simple scheme was used for cooling: after placing the sample in position near the tip, the scanning head was lowered from the laboratory air directly into a liquid helium reservoir.

Although these preliminary experiments enjoyed some success,[10] the majority of samples showed very poor tunneling characteristics after being cooled. We believe that the unavoidable period of exposure to air, ~10 minutes for these measurements, resulted in unacceptable surface contamination. The fact that this contamination persisted despite our efforts to protect the surface with inert overlayers highlights the importance of surface cleanliness for CSTM. Depending on the amount of air exposure, metal surfaces may acquire one or more monolayers of absorbates (e.g., oxides, water) which are largely transparent to room-temperature STM. Although it seems improbable that the STM would work at all with the tunneling tip poking through this layer of dirt, indirect

evidence suggests that this commonly occurs.[11] As long as the layer is insulating and the tunneling tip can move through it without being altered, there is little degradation of the STM performance. We believe that in our case such a layer would freeze solid upon cooling and severely affect the delicate tunneling tip. This caused extremely unstable behavior when performing CSTM even though atomic-resolution imaging was often possible on the same samples at room temperature.[12] Clearly, a suitable CSTM system would allow a sample to be prepared and probed while avoiding the contamination which results from exposure to air.

To keep the sample sufficiently clean, the design of our CSTM system would need to include *in-situ* cleaning and modification of the superconducting samples. The system would need to be operable from room temperature down to ~1 K, in order to perform topographic and spectroscopic measurements near the relevant transition temperatures and to achieve an energy resolution ~100μV. Furthermore, the desire to probe structures of nanometer size scale demands atomic resolution. Lastly, the capability to apply a magnetic field would be useful, as future plans include experiments that will probe superconductor magnetic flux structures.

2.2.2 System design

To satisfy our criteria, we constructed a CSTM system operable from room temperature to 1.5 K with an integrated sample preparation chamber.[13] Both the sample and the tunneling tip can be cleaned and/or modified in a UHV processing chamber which is connected to the top of a liquid-helium flow cryostat. Figures 2.5 and 2.6 show photographs and schematics of the system respectively, with the processing chamber oriented to the right of the cryostat. The system features a compact STM scanning head mounted to a threaded rod inside the sample tube of the cryostat. This allows the scanning head to be translated vertically from the top position, where a newly prepared

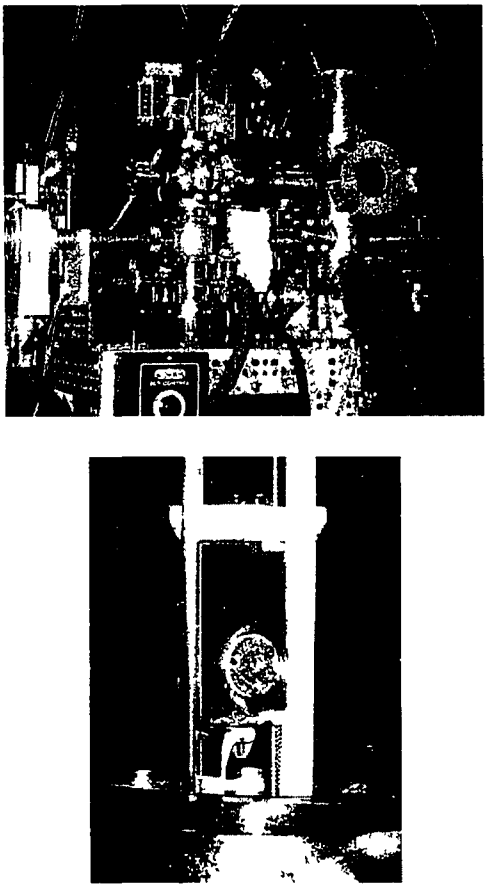

Fig. 2.5 Photographs of our cryogenic system. The top picture shows the cryostat and adjacent processing chamber, situated to the right. At bottom is the STM scanning head mounted to its vertical-translation assembly.

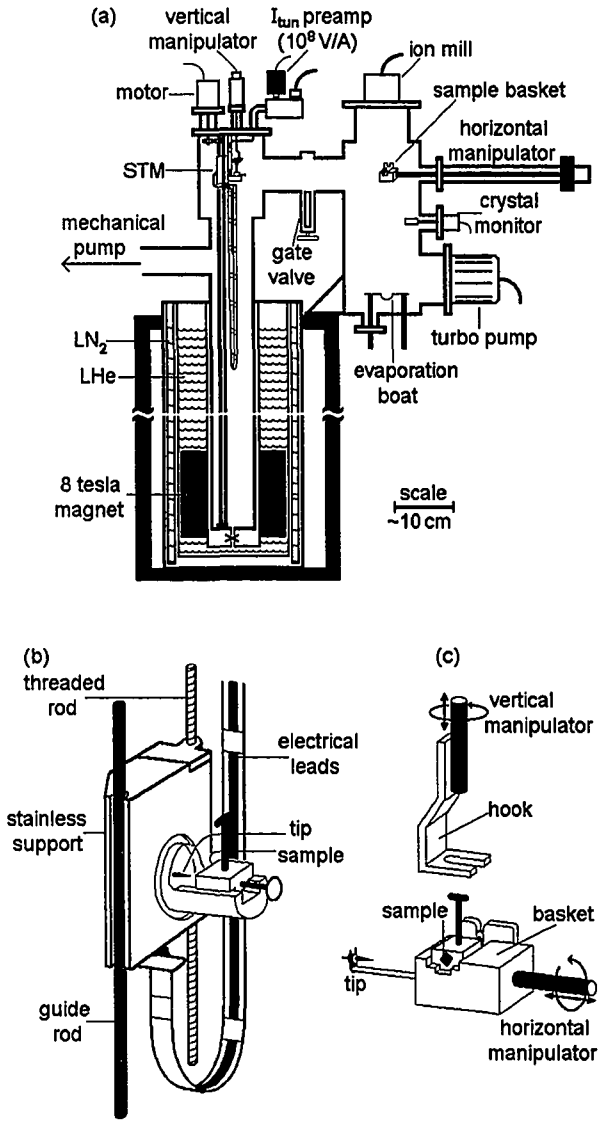

Fig. 2.6 (a) Sketch of our cryogenic system drawn roughly to scale. (b) An enlargement of the scanning head and vertical-translation assembly. (c) An enlargement of the fittings used for sample manipulation.

sample from the processing chamber can be transferred, to the bottom position, where it can be operated cryogenically. In this way, *in-situ* sample preparation can be performed to minimize surface contamination. The cryostat includes a superconducting solenoid capable of applying magnetic fields as great as 8 T. Because the system currently employs a horizontally-oriented scanning head, the direction of the applied field lies parallel to the sample surface. To accommodate an experiment which required a perpendicular field, a vertically-oriented scanning head could be incorporated.[14]

The 43 cm high x 15 cm diameter stainless-steel processing chamber is designed to allow for the deposition of thin films by sputtering and thermal evaporation, and for the cleaning of the surfaces by ion milling.[15] The sample (or substrate) is attached to the side of a sample holder block, which can be loaded into a Teflon sample basket. The basket is fitted to a horizontal rotary/linear manipulator, as shown in Figure 2.6(a,c). This allows the sample holder to be turned so that the sample faces any one of three ports on the top, back, or bottom of the chamber. These three ports hold the ion mill, sputter gun, and evaporation boats respectively, with the space in front of the sample basket reserved for a viewport/door. The orientation of the sample basket with respect to the scanning head also allows manipulation of tunneling tips. The chamber is equipped with a 240 l/s turbomolecular pump providing an ultra-high-vacuum environment $\sim 10^{-9}$ torr.

The processing chamber is coupled directly to the helium cryostat through a gate valve, as indicated in Figure 2.6(a). Because some components of the cryostat are vacuum coupled with Viton o-rings and gaskets, the system typically attains pressures $\sim 10^{-7}$ torr with the gate valve open. In order to transfer a newly prepared sample onto the scanning head, two rotary/linear manipulators are used. The long horizontal manipulator can translate the basket to the cryostat top, where it is positioned directly beneath a second vertically-oriented manipulator at the top of the cryostat. This manipulator is equipped with a hook that can latch on to the sample holder so that it can be lifted off the

basket, rotated 90° (the sample now facing the tunneling tip), and lowered into position near the tip.

The scanning head is mounted on a captive Acme threaded rod which is coupled to a dc gear motor via a direct-drive feedthrough (see Figure 2.6) so that it can be moved vertically throughout the sample tube of the cryostat. The electrical leads (12 low-heat-leak stainless-steel coaxial cables) are tethered to a phosphor-bronze support strip which constrains them to follow the STM's motion in a controlled way. Following the behavior of a common metallic tape-measure, a curvature introduced across the width of a 1.3 cm x 0.16 mm x 150 cm strip of this non-magnetic, low thermal-conductance alloy gives it a tendency to stay straight along its length. Such a strip is attached so that it drapes beneath the support block that holds the scanning head, with straight sides and a well-defined loop at the bottom, as shown in Figure 2.6(b). We attach the electrical leads to this strip by wrappings of Teflon tape every few centimeters, which easily slide along the inner surface of the sample tube. The bottom loop is used to hold the extra length of leads, which is necessary to move the scanning head downward from the top position. In this way, the scanning head with a newly prepared sample in place can be lowered to the bottom of the cryostat. Once the system has been cooled, however, we find that the scanning head must remain stationary due to the insulation in the coaxial leads. Below 100 K, this material becomes too stiff to safely bend around the bottom loop without the risk of cracking.

A He^4 flow cryostat[16] was chosen that enables the tip/sample temperature to be varied either by helium gas flow (300 K to 1.8 K) or by immersion in liquid helium (4.2 K to 1.5 K). In order to reach temperatures below 4.2 K, the sample tube of the cryostat is evacuated with a 66 l/s mechanical pump. Although the pump is only used when vapor is flowing or when the STM is immersed in liquid helium, a liquid nitrogen cold trap is installed in the pumping line to insure that no oil backstreams into the cryostat sample tube. The direct contact between the tip/sample and the helium gives a large cooling

power, which allows us to reach these low temperatures despite the multiple leads to the scanning head.

The scanning head is a compact design which easily fits inside the 5.7 cm inner diameter of the sample tube. Its normal modes of vibration are high frequency, resulting in relatively low sensitivity to building vibrations (see section 2.2.3). However, because it is rigidly coupled to the rest of the system, good vibration isolation is important to achieve a stable tunneling signal. We isolate the system from floor vibrations by resting it on four air springs inflated to 30 PSI and stacking 400 kg of lead bricks onto the base. In order to eliminate vibrations from the mechanical pump (located 10 m away from the cryostat), the final vacuum connection is made to the system with flexible rubber vacuum tubing. To reduce coupling to acoustical noises in the lab, the system is surrounded with sound-damping foam-rubber panels.[17]

The tunneling current is detected using a current-to-voltage preamplifier[18] mounted directly to the top of the cryostat to minimize the effects of electromagnetic interference. Most of the measurements presented in this work were obtained using custom-built control electronics, although the more recent data were taken with a commercially purchased unit.[19] Both systems feature standard feedback and scan-control circuitry, interfaced with a personal computer through a data acquisition board (see section 2.1.1 and Figure 2.2). The high-voltage output to the scanning piezoelectric tube has a maximum range of ±250 V yielding a scan range of 5 μm at 300 K and 0.6 μm at 1.5 K.

2.2.3 Scanning head design

At the heart of the system is a horizontally-oriented thermally-compensated STM scanning head designed by Lyding *et al.*[20] The scanning head has a compact length of only 3.8 cm and a rigid design which result in very high normal-mode vibration

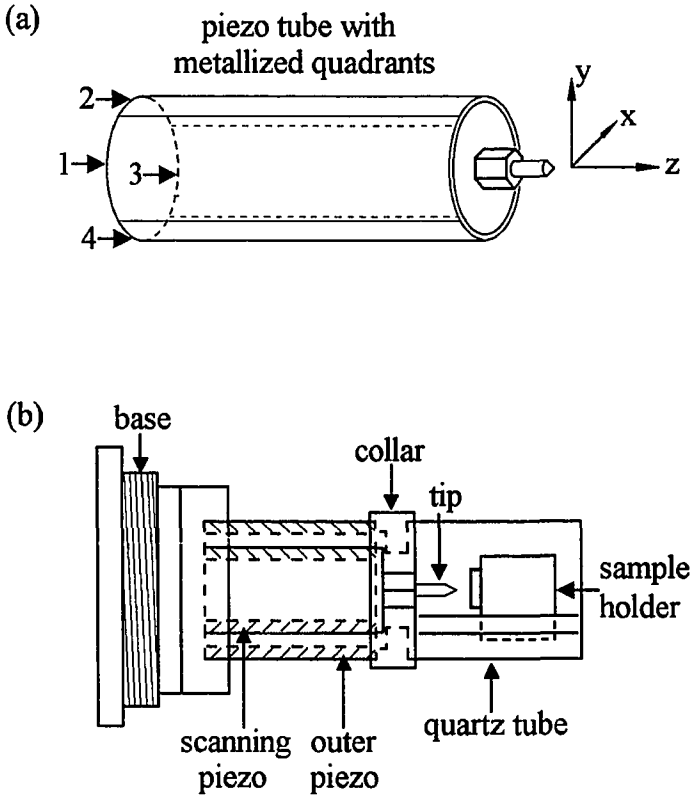

Fig. 2.7 Diagram of the piezoelectric scanning tube used in the Lyding-design STM.[20] The outer metallization defines four quadrants, labeled 1-4, to produce the tunneling tip's three-dimensional motion. (b) Complete schematic of the Lyding-design. Thermal compensation is achieved by supporting the sample with a second piezoelectric tube (labeled outer piezo).

frequencies, greater than 20 kHz. This compact and rigid design utilizes piezoelectric tubes made from a ceramic material commercially known as PZT-5H. The scanning tube is uniformly metallized on its inner surfaces, but has four independent quadrants of metallization on its outer surface, as indicated in Figure 2.7(a). The tunneling tip is mounted coaxially at one end of the tube, while the other end is firmly anchored to a base. With the inside electrode of the tube grounded and a voltage applied to one of the four outer electrodes, the wall thickness of the quadrant will increase (or decrease). Because the material conserves its total volume, the length of the quadrant decreases (or increases). Full range of motion in the x, y, and z directions can then be accomplished, as described in section 2.1.1.

The major innovation of the Lyding design is a geometry that minimizes displacements of the tip relative to the sample due to temperature fluctuations, a phenomenon known as thermal drift. This is accomplished by supporting the sample stage with a second piezoelectric tube, of equal length to the scanning tube. The two tubes are coaxially anchored to the same base, as shown in Figure 2.7(b). With this geometry, length changes of the scanning tube due to thermal expansion or contraction are matched by equal changes of the outer tube; thus thermal compensation in the z direction is achieved. With regards to the lateral directions, coaxial mounting of the tip and sample assures minimal displacement due to thermal drift.

In addition to thermal compensation, the outer tube provides the motion necessary to bring the sample into tunneling range by means of inertial translation. The sample stage consists of a sample holder block which can slide with little friction along a grooved quartz support tube; quartz was chosen for its negligible expansion properties. Now, low frequency voltage waveforms applied to the outer tube cause the sample holder to oscillate in z. But if the frequency is increased to several kHz, the static-friction limit is exceeded due to the inertia of the sample holder. This prevents it from following the motion of the support tube, and the sample holder remains stationary. The trick to getting

the sample holder to "walk" towards the tip is to apply an asymmetric waveform, such as a sawtooth. The sample holder will follow the support tube's motion during the slow portion of the signal, but will remain stationary during the fast portion. In this way, the sample slips a small distance, causing a net translation, typically ~500 Å.

Of course, it is important to prevent the sample from walking too far and coming into mechanical contact with the tip, a phenomenon known as crashing. This is easily accomplished by stopping the sawtooth as soon as any tunneling current is detected by the preamplifier. The feedback signal to the scanning tube will then adjust the z position of the tip, resulting in the desired amplitude for tunneling current. For the purpose of electrical contact to the sample, the upper surface of the support tube is metallized as are contact pads on the bottom of the sample holder. These metallized surfaces must be well polished and clean to insure that the inertial translation will work reliably during cryogenic operation.

2.2.4 Operation

In a typical data run the cryostat sample tube is first purged with nitrogen gas and evacuated with a mechanical pump to a pressure of a few hundred millitorr (with the gate valve shut). The sample holder is then loaded into the processing chamber and placed in the sample basket. By evacuating the processing chamber with the turbomolecular pump, the sample surface can be prepared in a UHV environment. Once the sample is ready, the gate valve is slowly opened so that the sample tube of the cryostat is evacuated. The sample holder is then transferred onto the scanning head and subsequently lowered down the sample tube to the cryostat bottom.

We have found that precooling the system while the sample tube is filled with an exchange gas causes unnecessary contamination of the sample surface. The problem is that contaminants drawn from the warmer stainless steel walls near the top of the cryostat

are then cryopumped downward to the sample. The surface is kept much cleaner by continuing to evacuate the sample tube with the turbo pump as liquid nitrogen is introduced into the cryostat reservoirs (with the needle valve connecting the sample tube to the helium reservoir shut). This allows the scanning head to precool by radiation in a high-vacuum environment $\sim 10^{-7}$ torr. The resulting low temperature gradient (0.2 °/min) minimizes thermal-contraction stresses on the STM which can significantly shorten its operating lifetime.

When the STM reaches around 150 K, liquid helium is introduced into the cryostat. The gate valve is then shut and the turbo pump switched off as further cooling is achieved by helium vapor rising through the needle valve at the bottom of the sample tube. Again, to avoid high thermal stress on the STM, the vapor flow rate is adjusted so that cooling proceeds at ≈ 0.7 °/min. Therefore, we take about 16 hours in total to cool a newly prepared sample to liquid helium temperatures. For temperatures at or below 4.2 K, we have achieved the best results by immersing the tip and sample in liquid helium. This environment provides excellent temperature stability while freezing out any residual contaminants. In practice, tunneling through liquid helium (an insulator) is much like vacuum tunneling. Due to the long cooling time, the system is not suitable for atomic-resolution applications involving reactive surfaces. However, by the use of samples which are chemically inert, such as PbIn, $NbSe_2$, graphite, or noble metals, the cleanliness of the surface can be maintained, allowing atomic resolution.

Once the desired cryogenic temperature has been reached, there are a variety of ways in which the sample can be characterized. The data presented in this work were obtained using two modes of operation which directly yield the relevant information: the constant-current scanning mode, and the spectroscopic mode. As described in section 2.1.1, the constant-current mode provides an atomic-resolution topographical image of the surface by rastering the tip while maintaining a constant tip-sample separation. In addition to identifying prepared structures on the surface, the topographical data can

indicate if the atomic lattice of the substrate is obscured by absorbates, serving as a good test of the surface quality. The software that controls the scanning also allows spectroscopic measurements to be taken concurrently at discrete points. This is accomplished by momentarily interrupting the scan at selected x,y points, while turning off the feedback to fix the z position of the tip. As discussed in section 2.1.3, the complete density of states of the surface $N(E=eV,x,y)$ can be obtained by measuring the local dI/dV while ramping the bias voltage V through the range of interest (as long as eV stays much less than the Fermi energy and the tip/sample workfunctions).

As opposed to measuring I versus V and then numerically taking the derivative, we take advantage of the noise rejection capability of a lock-in amplifier to immediately get dI/dV. Following the usual scheme, a small sinusoidal voltage is superimposed on the relatively slow V ramp. The resulting ac tunneling current, which has an amplitude proportional to dI/dV, is the input to the lock-in amplifier. As the output of the lock-in is proportional to amplitude of the input at the driving frequency, a dc signal proportional to dI/dV is obtained. This procedure, which typically takes about a minute per voltage ramp, demands very high stability: a constant tip-sample separation must be maintained to a precision ~0.01 Å without the use of feedback. To get reproducible spectroscopic data, the mechanical quality of the tip must be excellent, and special attention must be given to the vibration isolation features of the system.

We have found our system capable of high-quality topographical and spectroscopic measurements at both room temperature and cryogenic temperatures. Variable temperature operation is demonstrated in Figure 2.8. The sample is $NbSe_2$ which has distinct electronic features. It undergoes two phase transitions: a charge density wave (CDW) transition at 33 K, and a superconducting transition at 7 K. The charge density wave with a period of approximately three atomic spacings adds a modulation to the topographic images, as shown in Figure 2.8 (top). In terms of the electronic structure, each of the phase transitions gives rise to a respective energy gap in

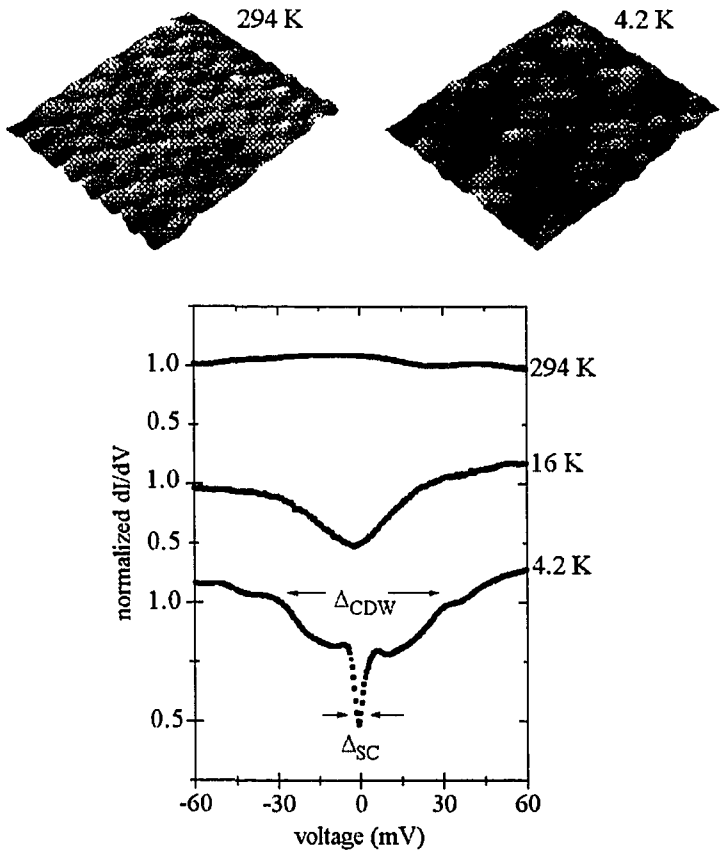

Fig. 2.8 Demonstration of variable temperature operation on $NbSe_2$. (Top) Two 30 Å x 30 Å topographic images showing atomic resolution at room temperature and additional CDW corrugations below the CDW transition temperature. (Bottom) Spectroscopic data showing the appearance of both a CDW gap (Δ_{CDW}) and a superconducting gap (Δ_{SC}) about the Fermi level, as the temperature is lowered.

the density of states. The spectroscopic curves shown in Figure 2.8 (bottom) display features of both the CDW gap and the superconducting gap, as indicated.

3. CSTM OF ISOLATED SUPERCONDUCTORS

3.1 BCS Relationships

In 1957, Bardeen, Cooper, and Schrieffer (BCS) produced their landmark theory of superconductivity,[21] which formed the basis for a majority of the ensuing theoretical work. In the BCS theory, it is shown that for temperatures below a critical value T_c a weak attraction can cause pairing between electrons near the Fermi level, resulting in a system which can be characterized as a macroscopic quantum state. Such an attraction can result from interactions with phonons, coupling electrons into so-called Cooper pairs, which comprise the superconducting charge carriers. We can understand how a phonon-mediated interaction can overcome the Coulomb repulsion between electrons in the following way. The bare Coulomb interaction between two electrons (1 and 2) inside a solid will be screened, by the other electrons and also by the positive ions in the lattice. In fact, the ions can have a very large response, effectively over-screening the negative charge of the electron. This results in a positive cloud in the vicinity of electron 1, which can then attract electron 2.[22] The following discussion is by no means intended to be a survey of the BCS theory.[9,22] Rather, select BCS relationships are introduced for comparison to measurements of isolated superconductors, and to provide a starting point for the later discussion of normal-metal / superconductor (NS) structures.

Because a large number of electrons participate in the superconducting state, the BCS ground state is most conveniently expressed using creation/annihilation operators. In this context, a term $c^*_{k\uparrow}c^*_{-k\downarrow}$ creates a Cooper pair consisting of a spin-up electron of momentum $\hbar k$ and spin-down electron of momentum $-\hbar k$. BCS took the form for the ground state wavefunction to be

$$|\psi_{BCS}\rangle = \prod_k \left(u_k + v_k c^*_{k\uparrow} c^*_{-k\downarrow}\right)|\psi_0\rangle,$$

where $|\psi_0\rangle$ is the vacuum state. The physically significant quantities $|v_k|^2$ and $|u_k|^2 = 1-|v_k|^2$ yield respectively the probability that the pair (k,-k) is occupied or unoccupied. The Cooper pairs have an extended nature, with a characteristic size set by the coherence length ξ. This quantity is typically ~3000 Å for low-T_c superconductors.

The BCS theory shows that the condensation of Cooper pairs lowers the energy with respect to the ordinary Fermi-sea ground state. The theory also shows that the energy of the system can be increased by fermion elementary excitations which are referred to as quasiparticles. Relative to the Fermi energy E_F, the energy of a quasiparticle of momentum $\hbar k$ is given by

$$E_k = \sqrt{\varepsilon_k^2 + |\Delta_k|^2},$$

where Δ_k is referred to as the pair potential, and $\varepsilon_k = (\hbar^2 k^2/2m) - E_F$. Because even at the Fermi surface $E_k = |\Delta_k| > 0$, Δ_k represents an energy gap in the quasiparticle density of states. For the solution to be self-consistent, Δ_k must satisfy the condition:

$$\Delta_k = -\sum_l g_{kl} u_l^* v_l \left[1 - 2f(E_k)\right] \qquad 3.1$$

where g_{kl} is the matrix element for the attraction between electronic states k and l, and f is the usual Fermi function $f(E_k) = 1/(e^{E_k/k_B T} + 1)$.

We conclude this section with three relationships that assume a weak attractive interaction, independent of k, for a homogeneous superconductor which is well below T_c and in the absence of a magnetic field. In this case, g_{kl} can be replaced with an effective

interaction constant $g<<1/N_0$, where N_0 is the normal-state density of states (assumed constant as we are interested in energies only a few meV from E_F). Δ_k can then be taken as a positive real constant, which we designate as the bulk energy gap Δ_∞. Measuring energies with respect to the Fermi level, the BCS density of states can be written as

$$\frac{N_{BCS}(E)}{N_0} = \begin{cases} \dfrac{E}{\sqrt{E^2 - \Delta_\infty^2}}, & E > \Delta_\infty \\ 0, & E < \Delta_\infty \end{cases} . \qquad 3.2$$

As shown in Figure 3.1, the absence of quasiparticle states inside the gap is compensated for by enhanced densities beyond the gap. In fact, the total number of levels is the same as for the normal state. We can also express the coherence length in terms of Δ_∞,

$$\xi_{BCS} = \frac{\hbar v_F}{\pi \Delta_\infty}, \qquad 3.3$$

where v_F is the Fermi velocity. Lastly, we give the famous BCS relationship between the zero temperature energy gap and the critical temperature: $\Delta_\infty = 1.76\, k_B T_c$.

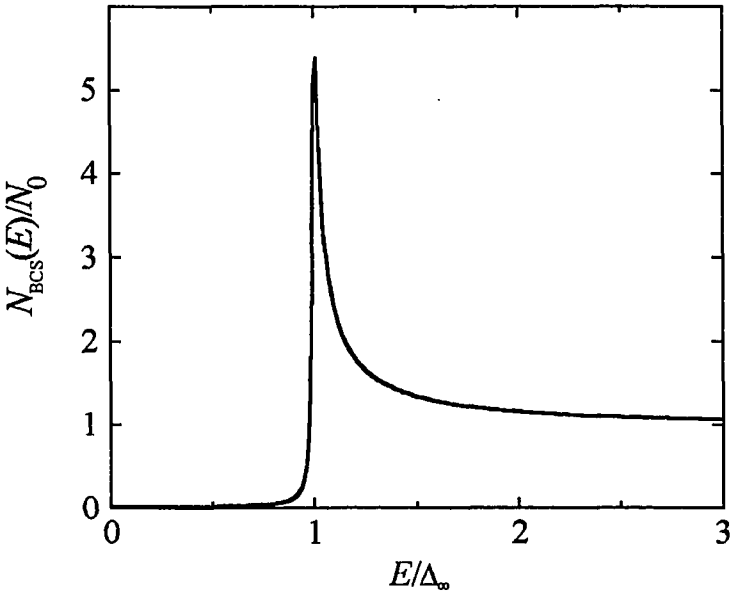

Fig. 3.1 The BCS density of states $N_{BCS}(E)$. The curve is broadened slightly to remove the divergence at $E=\Delta_\infty$.

3.2 Measurements

Before presenting the results of density of states measurements of NS structures, it is expedient to first address CSTM spectra of isolated superconductors. We have performed such measurements on both single crystals and polycrystalline films using $NbSe_2$, Nb, and Pb-In. This represents an important test of the capabilities of our cryogenic system to obtain reproducible measurements on the scale of the energy gap. Of course, of equal importance is to determine the limitations of CSTM spectroscopy. Similar results are obtained for each of the tested superconductors; here we show spectra from two samples immersed in liquid He at 1.6 K: $NbSe_2$ and Pb-In.

We first demonstrate spatial reproducibility on the homogeneous surface of $NbSe_2$, an anisotropic layered superconductor with a T_c of 7 K. Cleaving a crystal parallel to the layers with Scotch tape allows a fresh, atomically-flat surface to be exposed, as shown in Figure 2.8. Single crystals were grown using an iodine-assisted transport reaction in a gradient furnace.[23] The material is chemically inert, allowing for negligible contamination during the few minutes of air exposure between the cleave and subsequent placement into the vacuum system. Figure 3.2 shows (a) 16 consecutive dI/dV vs. V curves taken on $NbSe_2$ at different locations, and (b) an enlargement of a representative curve. All the measurements have been normalized to the value observed at high voltage. The sampled locations form a 4 x 4 square grid with a nearest neighbor spacing of 20 Å as indicated. We clearly see gap-like spectra, reminiscent of the BCS energy gap, which is approximately the same at each location, as expected. However, the data show a background slope which varies from curve to curve (this slope is most evident in the (x,y)=(60 Å, 60 Å) curve). In fact, this effect is not a reproducible function of position, but appears to be random in time. We believe that we are simply observing the results of a gradual thermal drift on the μK scale, which induces changes to the tip-

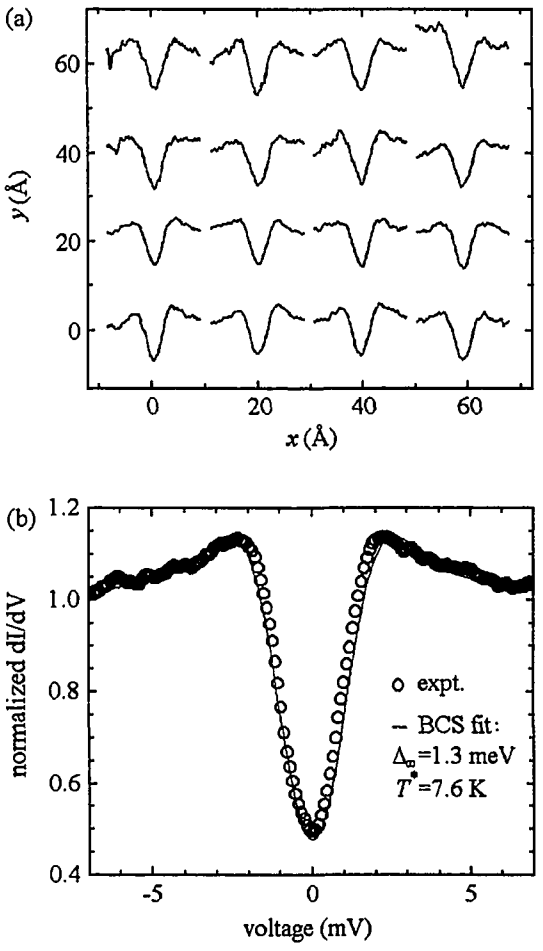

Fig. 3.2 (a) Sixteen measurements of dI/dV vs. V taken at different relative (x,y) position on the a $NbSe_2$ crystal, as indicated. (b) An enlargement of a representative measurement compared with a BCS curve.

sample spacing σ of a few mÅ. To correct for this, we routinely subtract a background slope from the data after normalization, as was done for Figure 3.2(b).

We can further check if the gap-like curves are consistent with BCS theory by comparing them to N_{BCS}. We accomplished this using Eq. 3.2, adding the reflection on the negative-energy side. (The resulting density of states will then reduce properly to the normal metal density of states as $\Delta_\infty \rightarrow 0$.) Next, the curve is thermally broadened via Eq. 2.2, resulting in a simulated dI/dV vs. V curve. As shown in Figure 3.2(b), the BCS density of states, with Δ_∞=1.30 meV, reproduces excellently the measured dI/dV. This is consistent with previous CSTM measurements of $NbSe_2$ taken at millikelvin temperatures, which show a gradual onset of conduction at ±0.7 mV and peaks at ±1.3 mV, indicating a distribution of energy gaps from 0.7 to 1.4 meV.[24]

However, the measured dI/dV is smeared energetically much more than it should be, as to achieve a good fit, the effective broadening temperature T^* must be taken to be 7.6 K, a value much greater than the bath temperature of 1.6 K. Alternatively, the measurements could be fit using the experimental temperature by incorporating a phenomenological lifetime broadening term.[25] While the intrinsic distribution of energy gaps in $NbSe_2$ may account for some of the discrepancy, perhaps 1 K, the remaining source of broadening is unknown. In fact, this phenomenon is not limited to $NbSe_2$, as it has been consistently observed it to some degree in all CSTM spectroscopic measurements. In most cases, the extra smearing is blamed on the high current density inherent to STM.[6] This could result in non-equilibrium breaking of Cooper pairs which would alter the density of states.

If, indeed, the tunnel current were responsible for the energy smearing, the extent of the smearing should be a function of the current density. We have tested for current density effects using films of superconducting Pb-In alloy (T_c=7 K). This material allows for stable tunneling characteristics while varying the tip-sample spacing (σ) over a range of about 3 Å, enough to achieve a three orders of magnitude variation in the current

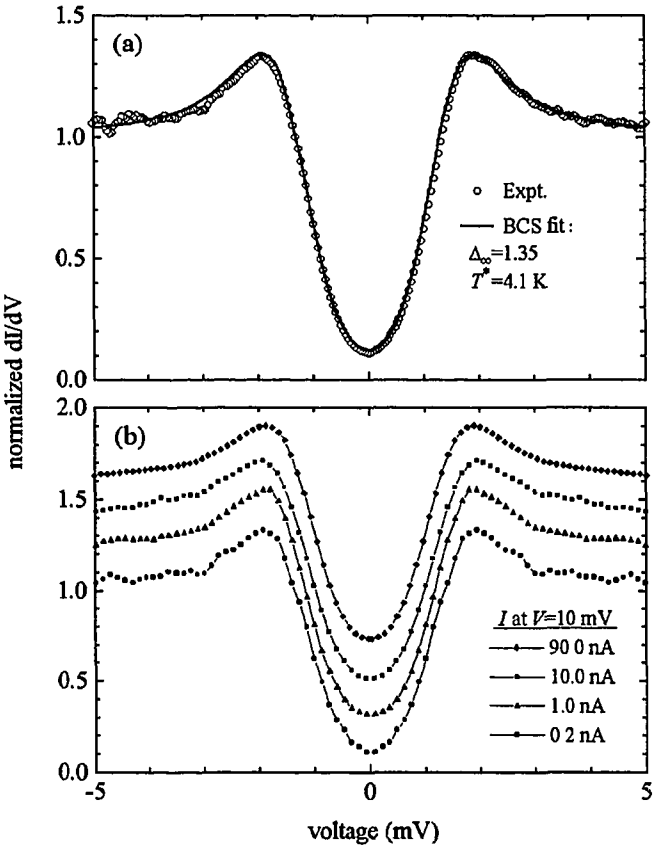

Fig. 3.3 (a) A representative spectroscopic measurement of Pb-In fit with a BCS density of states as indicated. The tunnel current at 10 mV was 0.5 nA. (b) Four successive measurements taken at the same location, but with a different current. Successive curves have been shifted upward for clarity.

density. In contrast, attempts to vary σ over a significant range with $NbSe_2$ result in an unstable current; the difficulties probably arise from tip-sample interactions which can exert forces on the loosely-coupled layers. The samples were prepared *in situ* by coevaporation of Pb and In (20%) to a thickness of 1000 Å on a graphite substrate. Figure 3.3(a) shows a typical dI/dV curve fit with the BCS density of states; the best-fit parameters are Δ_∞=1.35 meV and T^*=4.1 K as indicated. Once again, an excellent fit is achieved using an energy gap approximately consistent with the accepted value,[26] but with an effective temperature much greater than the experimental one of 1.6 K. Figure 3.3(b) shows four additional spectra taken at the same location and with the same tip (chemically etched Pt-Ir) as the spectrum shown in (a). As indicated, σ has been adjusted for each successive curve to increase the tunnel current by an order of magnitude. Assuming a tunneling area of 10 $Å^2$, this corresponds to a variation of the current density at 10 mV from 2 x 10^5 A/cm^2 to 9 x 10^7 A/cm^2. To reduce scatter, the positive and negative branches of each spectrum have been averaged together. We see that despite the 450-fold current increase, there is no discernible change in the normalized dI/dV.

We conclude that CSTM spectra of isolated superconductors consistently yield the expected BCS density of states. We believe that it is unlikely that the extra, non-thermal energy smearing arises due to the STM's high current density, as we find no current-density dependence over a three order of magnitude range.

Another possible source of the energy smearing is a manifestation of the uncertainty principle. The effect could arise from the confinement of electrons to the narrow channel during the STM tunneling process. Assuming this constitutes a quantum-mechanical determination of the electronic positions, there should be an accompanying smearing of the energies. However if this were the case, the uncertainty principle must be at work in a subtle way. For example, taking the diameter of the tunneling channel to be ~10 Å, a straight-forward application of the relation $\Delta x \Delta p \sim \hbar$ leads to an uncertainty in energy of roughly 1 eV. But we consistently observe much less energy broadening

~ 1 meV. Clearly, the source of the non-thermal energy smearing in STM spectra remains an open question.

4. THEORY OF BOUND STATES IN NORMAL/SUPERCONDUCTOR (NS) STRUCTURES

4.1 Bogoliubov-de Gennes (BdG) Equations and the Superconducting Proximity Effect

If a superconductor is placed in electrical contact with another metal, or in a magnetic field, the pair potential Δ will vary in space. A framework to calculate the quasiparticle properties in these situations is provided by the Bogoliubov-de Gennes (BdG) equations, which can be viewed as a generalization of the Schrödinger equation for single-particle excitations in a superconducting system. In this section we introduce the BdG equations and their relevant parameters. As the equations are based on BCS theory, this brief discussion will refer to analogous quantities introduced in Sec 3.1.

The standard derivation[22] begins by recasting the problem in terms of position eigenfunctions $u(\boldsymbol{r})$ and $v(\boldsymbol{r})$ instead of the momentum eigenfunctions $u_{\boldsymbol{k}}$ and $v_{\boldsymbol{k}}$. In this case the u and v correspond to quasiparticle excitations, with $|u(\boldsymbol{r})|^2$ and $|v(\boldsymbol{r})|^2$ yielding respectively the probability for finding a quasielectron and quasihole at location $\boldsymbol{r}$. Creation and annihilation operators are defined with respect to the new u and v, and $\Delta_{\boldsymbol{k}}$ is replaced in favor of the spatially dependent pair potential $\Delta(\boldsymbol{r})$. The BdG equations then follow as the requirement for diagonalization of the original hamiltonian:

$$\begin{aligned} \varepsilon u(\boldsymbol{r}) &= \mathcal{H}_0 u(\boldsymbol{r}) + \Delta(\boldsymbol{r}) v(\boldsymbol{r}) \\ \varepsilon v(\boldsymbol{r}) &= -\mathcal{H}_0^* v(\boldsymbol{r}) + \Delta^*(\boldsymbol{r}) u(\boldsymbol{r}) \end{aligned} \quad , \qquad 4.1$$

where $\mathcal{E}$ is a positive energy eigenvalue, and $\mathcal{H}_0$ is the hamiltonian for the system in the absence of pairing, with energies measured relative to E_F. In analogy to Eq. 3.1, $\Delta(\boldsymbol{r})$ is required to follow a self-consistency condition[27]

$$\Delta(\boldsymbol{r}) = g(\boldsymbol{r})\sum_n v_n^*(\boldsymbol{r})u_n(\boldsymbol{r})\left(1-2f(\mathcal{E}_n)\right) \equiv g(\boldsymbol{r})F(\boldsymbol{r}), \qquad 4.2$$

where $g(\boldsymbol{r})$ is the effective interaction parameter, and $F(\boldsymbol{r})$ is the condensate amplitude.

It is illuminating to apply the BdG equations to the case of a normal metal, for which $\Delta(\boldsymbol{r})=0$ for all $\boldsymbol{r}$. Eqs. 4.1 then decouple into two independent Schrödinger-like equations: one for u with eigenenergy above the Fermi level, and one for v with eigenenergy below the Fermi level. Clearly, these eigenfunctions play the role of quasiparticle wavefunctions, with u and v being the electron and hole wavefunctions respectively.

Returning to Eq. 4.2, we see that the spatial variation of the pair potential is constrained by F and g. This relationship is fundamental to the understanding of the superconducting proximity effect, a phenomenon that occurs when a superconductor (S) comes into contact with a normal metal (N). As F is a measure of the local pair density, it cannot vary discontinuously across the interface due to the extended nature of the Cooper pairs. Instead, some paired electrons leak across the boundary, so that F falls off smoothly. This results in a weakening of superconductivity in S, and induced superconductivity in N. F varies with distinct length scales in the two materials, ξ_S and ξ_N; ξ_S is the superconducting coherence length introduced in Sec. 3.1, while the normal-metal coherence length ξ_N is given by $\hbar v_{FN}/k_B T$ in the clean limit. For systems with typical coherence lengths, greater than 300 Å, g can vary rapidly compared to F, depending mostly on the local materials properties. For this reason, the conventional picture of the proximity effect allows g to vary discontinuously at the SN interface. So if

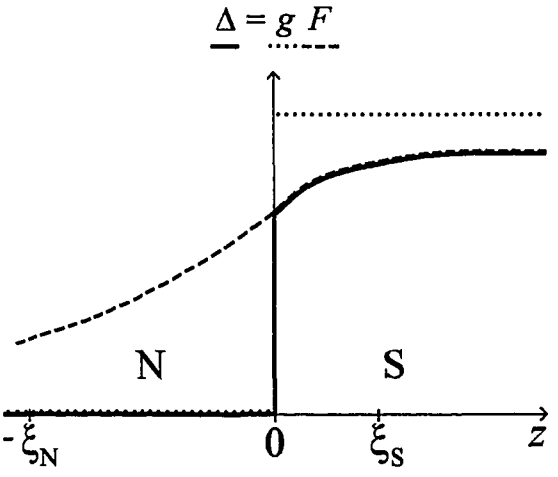

Fig. 4.1 The conventional picture of the proximity effect in which it is assumed that g can vary rapidly on the scale of ξ_S and ξ_N. Here we show the behavior of Δ (solid) and F (dashed) in the case of g_N=0 and g_S=1, as indicated by the step function (dots).

g_N=0, there will be no induced pair potential in N, despite the presence of superconductivity (as measured by F), as shown in Figure 4.1.

For the case of short-coherence-length superconductors, allowing g to vary discontinuously may become a poor approximation. Microscopically, g must be continuous, with the length scale for significant variations set by a characteristic length ξ_g. As described in Sec. 3.1, the attractive interaction responsible for pairing in the low temperature superconductors arises from screening effects. For this reason, ξ_g is expected to be of order of the charge screening length, or the inverse of the Fermi wave number, $1/k_F$.[22] If the coherence length of the superconductor is short enough so that it approaches ξ_g, then to properly describe the situation at an SN interface, the detailed form of g must be considered in addition to F. This behavior represents a significant departure from the conventional picture, and has not been observed experimentally prior to this work. But the atomic scale spectroscopic capability of CSTM applied to such an SN interface allows for the possibility to detect the presence of a significant ξ_g.

4.2 de Gennes-Saint-James (dG-SJ) Model

In a concise and elegant 1963 paper, de Gennes and Saint-James applied the BdG equations to the case of a normal-metal slab N of finite thickness in electrical contact with a semi-infinite superconductor S.[28] They predicted that there will be quasiparticle states bound in the N layer due to the local reduction in Δ, giving rise to discrete states. Ten years later, the existence of quasiparticle bound states in planar NS structures was verified by experiments, which identified the bound-state peaks in the density of states by tunneling through an oxide-barrier.[29] Although refinements to the original work have been made by other theorists,[30,31] the standard theory of quasiparticle behavior in NS structures will be referred to as the de Gennes-Saint-James model (dG-SJ).

Before embarking on a detailed discussion of quasiparticle bound states based on the BdG equations, we can get an intuitive understanding of the physics by considering the fate of an electron inside N. (A thorough introduction can be found in reference 32.) If the energy of the electron is below the gap of S, it costs energy for it to exist there as unpaired free particle. Therefore, at the NS interface it will be reflected in some way. In fact, the electron is reflected back into N as a hole as a result of the process known as Andreev reflection.[33] Assuming a long mean free path, this hole will return to the NS interface after a conventional reflection off the back N-vacuum wall. A second Andreev reflection converts the hole back into an electron, which will interfere with the original particle/wave. A discrete bound state can then be understood as meeting the conditions for constructive interference.

4.2.1 Bound state behavior

In the following discussion, we solve for the bound states in a simple, idealized system using the strategy employed by de Gennes and Saint-James.[28] In light of the lessons learned from bound states in vortices as described in Chapter 1, we extend the original calculation to solve explicitly for the bound state wavefunctions. This treatment yields good insight into the behavior of quasiparticle bound states, serving as guide for our intuition as we confront more realistic models for NS structures.

We begin with the simplifying assumption that the N layer, of thickness d_N, and the semi-infinite S layer share the same Fermi velocity v_F and effective mass m. We also restrict our attention to propagation perpendicular to the NS interface (z), which is the direction of confinement. The corrections introduced by considering trajectories parallel to the interface will be discussed in Sec. 6.2. The one-dimensional form for the BdG equations can then be used, where we let $\mathcal{H}_0$ be the free-electron-gas hamiltonian

$$\mathcal{H}_0 = -\frac{\hbar^2}{2m}\frac{\mathrm{d}^2}{\mathrm{d}z^2} - E_F .$$

Eqs. 4.1 become

$$\begin{aligned} \varepsilon u(z) &= -\left(\frac{\hbar^2}{2m}\frac{\mathrm{d}^2}{\mathrm{d}z^2} + E_F\right)u(z) + \Delta(z)v(z) \\ \varepsilon v(z) &= +\left(\frac{\hbar^2}{2m}\frac{\mathrm{d}^2}{\mathrm{d}z^2} + E_F\right)v(z) + \Delta(z)u(z) \end{aligned} \qquad 4.3$$

The dG-SJ model takes the pair potential to be a step-function with the discontinuity located at the interface (z=0) given by

$$\Delta(z) = \begin{cases} 0 & , -d_N < z < 0 \\ \Delta_\infty & , z > 0 \end{cases}, \qquad 4.4$$

where Δ_∞ is the real, non-negative pair potential which equals the energy gap of the isolated superconductor. To simplify the algebra, we assume Δ_∞ is much less than E_F throughout the analysis. No attempt is made to satisfy the self-consistency condition (Eq. 4.2), which amounts to neglecting corrections to Eq. 4.4 due to the proximity effect.

We now consider quasiparticle excitations inside the gap, $\varepsilon<\Delta_\infty$, which are forbidden to propagate freely into the superconductor. Beyond some characteristic length inside S the wavefunctions must vanish, analogous to the situation at a potential step in Schrödinger-equation quantum mechanics. Indeed, the following treatment closely parallels the textbook discussion of the familiar one-dimensional problem of a particle-in-a-box.[34] We start by identifying the form of the solution on each side of the interface. Because Δ=0 inside N, the quasiparticle wavefunctions u and v are independent, as

described in Sec. 4.1. We ensure that the wavefunctions vanish at the vacuum/N interface $z=-d_N$, by choosing solutions of the form

$$\begin{aligned} u(z) &= A\sin\left[k_u(z+d_N)\right] \\ v(z) &= B\sin\left[k_v(z+d_N)\right] \end{aligned} \quad , -d_N \le z \le 0, \qquad 4.5a$$

which is consistent with an infinite potential for $z \le -d_N$. An arbitrary phase can be added to the solution, just as for the particle-in-a-box problem; for simplicity, we choose A to be real (we will later see that this implies that B is also real). Now, inside S where $\Delta=\Delta_\infty$, u and v are coupled and must share the same exponent. Eq. 4.3 allows the exponent to be complex, resulting in oscillatory solutions within an exponential envelope: $e^{(\pm\kappa\pm ik)z}$, where κ and k are real. Because $u, v \to 0$ as $z \to +\infty$ in our case, we take the form to be

$$\begin{aligned} u(z) &= \alpha_1 e^{(-\kappa+ik)z} + \alpha_2 e^{(-\kappa-ik)z} \\ v(z) &= \beta_1 e^{(-\kappa+ik)z} + \beta_2 e^{(-\kappa-ik)z} \end{aligned} \quad , z \ge 0. \qquad 4.5b$$

Applying Eqs. 4.5 to Eqs. 4.3, we find that the k's and κ can be solved for in terms of $\mathcal{E}$ and the Fermi wave number $k_F = \sqrt{2mE_F}/\hbar$. Making use of $\Delta_\infty, \mathcal{E} \ll E_F$, we find

$$k_u = k_F + \frac{m\mathcal{E}}{\hbar^2 k_F} \quad , \quad k_v = k_F - \frac{m\mathcal{E}}{\hbar^2 k_F} \qquad 4.6$$

$$\kappa = \frac{m}{\hbar^2 k_F}\sqrt{\Delta_\infty^2 - \mathcal{E}^2} \quad , \quad k = k_F$$

From the requirement that u,v, du/dz, and dv/dz be continuous at the interface, z=0, we obtain the equation

$$\begin{aligned}&\left[(k+\mathrm{i}\kappa-k_u)e^{\mathrm{i}k_u d_N}-(k+\mathrm{i}\kappa+k_u)e^{-\mathrm{i}k_u d_N}\right]\left[(k-\mathrm{i}\kappa+k_v)e^{\mathrm{i}k_v d_N}-(k-\mathrm{i}\kappa-k_v)e^{-\mathrm{i}k_v d_N}\right]e^{\mathrm{i}2\phi}- \\ &\left[(k+\mathrm{i}\kappa-k_v)e^{\mathrm{i}k_v d_N}-(k+\mathrm{i}\kappa-k_v)e^{-\mathrm{i}k_v d_N}\right]\left[(k-\mathrm{i}\kappa+k_u)e^{\mathrm{i}k_u d_N}-(k-\mathrm{i}\kappa-k_u)e^{-\mathrm{i}k_u d_N}\right]=0,\end{aligned} \qquad 4.7$$

where the phase ϕ is defined as

$$\cos\phi=\frac{\varepsilon}{\Delta_\infty},\ 0\le\phi\le\frac{\pi}{2}\ . \qquad 4.8$$

The restriction of ϕ to the interval between 0 and $\pi/2$ serves two purposes: (1) it ensures that only states corresponding to $\Delta_\infty>0$ are considered, and (2) upon finding the bound-state solutions, it will prevent double-counting the number of states for a given d_N.

Eq. 4.7 greatly simplifies by making use of the following approximations, accurate to lowest order in ε/E_F:

$$k\pm\mathrm{i}\kappa+k_{u,v}=2k_F\ ,\ \ k\pm\mathrm{i}\kappa-k_{u,v}=0.$$

We then find

$$e^{\mathrm{i}2(k_u-k_v)d_N}=e^{\mathrm{i}2\phi},$$

so that

$$(k_u-k_v)d_N=\phi+n\pi\ ,\ n=\text{an integer}. \qquad 4.9$$

Using Eqs. 4.6 and 4.8, this can be rewritten as

$$\frac{2}{\pi}\frac{d_N}{\xi}\cos\phi = \phi + n\pi, \qquad 4.10$$

where ξ, the characteristic length scale for d_N, is

$$\xi = \frac{\hbar^2 k_F}{\pi m \Delta_\infty}.$$

More generally, the length scale for d_N is set by the materials parameters of the normal metal. But because the de Gennes-Saint-James model assumes the normal metal and the superconductor share the same k_F and m, this ξ is identical to the BCS coherence length in the superconductor, Eq. 3.3.

The solutions to Eq. 4.10 determines the number of bound states and their energies. For a fixed value of d_N, there is exactly one solution for each non-negative integer n such that

$$n \le \frac{2}{\pi^2}\frac{d_N}{\xi}. \qquad 4.11$$

Hence, the number of bound states increases with d_N/ξ, with at least one, corresponding to n=0, for any d_N>0. This follows the analogy with the textbook particle-in-a-box, for which larger potential wells hold more bound states, with a minimum of one. However, in our case the level spacing is roughly constant, as can be seen from Eq. 4.10: Designating the energy for each bound state as $\varepsilon_n = \Delta_\infty \cos\phi_n$, if both $\Delta_\infty/\varepsilon_n$ and d_N/ξ are much greater than one, we find

$$\varepsilon_n \approx \Delta_\infty \frac{\pi^2 \xi}{2d_N}(n+\tfrac{1}{2}).$$

We also label the bound-state wavefunctions for each state as u_n and v_n, with parameters k_{un}, etc., given by Eq. 4.6.

To complete the solution, the wavefunctions can be found explicitly by returning to the continuity requirements and solving for B, $\alpha_{1,2}$, and $\beta_{1,2}$ in terms of A, ϕ_n, and k_{un}. Eqs. 4.5 then become

$$u_n(z) = \begin{cases} A_n \sin[k_{un}(z+d_N)] & , \ -d_N < z < 0 \\ A_n e^{-\kappa_n z} \sin(k_n z + k_{un} d_N) & , \ z > 0 \end{cases}$$

$$v_n(z) = \begin{cases} (-1)^n A_n \sin[k_{vn}(z+d_N)] & , \ -d_N < z < 0 \\ A_n e^{-\kappa_n z} \sin(k_n z + k_{un} d_N - \phi) & , \ z > 0 \end{cases} \quad , \qquad 4.12$$

where A has been labeled A_n for use as the normalization factor for each state. The normalization requirement follows from the fact that $|u_n(z)|^2$ and $|v_n(z)|^2$ give respectively the probability for finding the bound-state particle and hole at location z. Because the state must be either a particle or a hole which can be found somewhere, the value for A_n is determined by the requirement

$$1 = \int_{-d_N}^{\infty} \left(|u_n(z)|^2 + |v_n(z)|^2 \right) dz.$$

We find

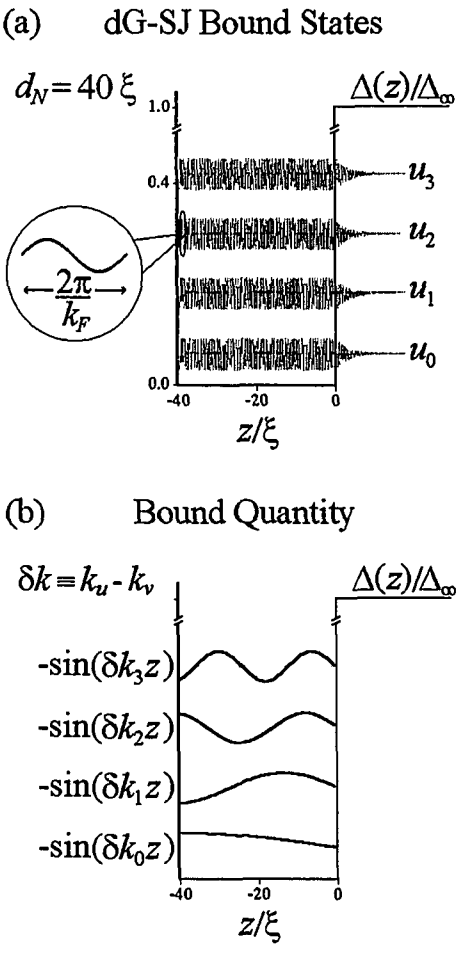

Fig. 4.2 (a) The 4 lowest-energy dG-SJ bound-state wavefunctions u_n for the case of d_N/ξ=40 (8 bound states in total). Only amplitude variations as a function of z are discernible, as the wavelengths of the oscillations are short on the scale of several ξ. (b) Waves constructed from the difference of particle and hole wave numbers. These quantities follow approximately the behavior of the particle-in-a-box wavefunctions of elementary quantum mechanics.

$$A_n = \frac{1}{\sqrt{\xi}}\left(\frac{d_N}{\xi} + \frac{1}{2\xi\kappa_n}\right)^{-1/2}. \qquad 4.13$$

Despite the simplicity of this expression, A_n is generally a complicated function of d_N, as κ_n can be found from Eq. 4.6 only after solving Eq. 4.10 for ε_n.

Figure 4.2(a) shows the low-lying quasiparticle wavefunctions at their respective energies, $\varepsilon_n << \Delta_\infty$, superimposed with the pair potential well for the case of $d_N/\xi=40$. It is clear that despite the analogy to the Schrödinger-equation particle-in-a-box, the bound wavefunctions have a very different character. In the case of the particle-in-a-box of width $L_\square$ and infinite potential walls, the bound wave numbers $k_\square$ are given by $k_\square L_\square = n_\square \pi$, where $n_\square = 1,2,...$[34] The resulting wavefunctions have integral numbers of half-wavelengths that fit inside the well, with nodes occurring at each boundary. In contrast, the wave numbers for the quasiparticle bound states, k_u and k_v, are set approximately by the Fermi wave number k_F irrespective of the well width. In Figure 4.2(a), the resulting wavelength is sufficiently small so that individual oscillations are not even discernible, and all the low-lying wavefunctions look about the same.

This comparison highlights the difference in the physics governing quasiparticle bound states. Unlike a Schrödinger well, a pair potential well is restricted to energies near the Fermi level, as it is essentially the energy-gap of the bulk superconductor. Only quasiparticles near the Fermi level are affected, with bound states forming as Andreev reflection mixes particles and holes. As a result, there is a wave number made up of both k_u and k_v that does follow roughly the particle-in-a-box behavior: $\delta k \equiv k_u - k_v$. Eq. 4.9 shows that δk follows a quantization condition similar to $k_\square$, except for an extra term of ϕ. For low-lying states $\phi \approx \pi/2$, so that waves can be constructed from δk which are similar to particle-in-a-box wavefunctions with an anti-node at the vacuum interface and a node at the superconductor interface, as shown in Figure 4.2(b). These constructed waves can

help guide our intuition for more complicated models, but it should be emphasized that they are not measurable wavefunctions like u_n and v_n.

4.2.2 CSTM measurements

With respect to experimental measurements, the quantity of interest is the local density of states,

$$N(E,z) = \sum_n \left[|u_n(z)|^2 \delta(E - \varepsilon_n) + |v_n(z)|^2 \delta(E + \varepsilon_n) \right]. \qquad 4.14$$

As described in Section 2.1.3, $N(E,z=-d_N)$ can be measured with CSTM by positioning the tip above the normal layer's surface. Strictly speaking, this quantity is equal to zero in the dG-SJ model due to the boundary condition $u_n(-d_N)$ and $v_n(-d_N)$ equal zero. However in practice, the presence of the tunneling tip perturbs the wavefunctions with respect to z, resulting in a non-zero surface value which is proportional to the amplitude inside the normal layer. From Eqs. 4.12, we see that both $|u_n(-d_N)|^2$ and $|v_n(-d_N)|^2$ will then be proportional to A_n^2. Writing $N(E,z=-d_N)$ as $N(E)$, Eq. 4.14 becomes

$$N(E) \propto \sum_n A_n^2 \left[\delta(E - \varepsilon_n) + \delta(E + \varepsilon_n) \right]. \qquad 4.15$$

So, local density of states measurements for $|E|<\Delta_\infty$ will yield the spectrum of bound states as δ-function peaks at $\pm\varepsilon_n$, with the relative magnitudes given by A_n^2.

Anticipating the experimental results, we focus on $d_N<\xi\pi^2/2$ in which case there is only the n=0 bound state. Figure 4.3 shows the normalization factor for this state A_0^2 calculated as a function of d_N. The gradual decrease as $d_N \to \infty$ is easy to understand: as

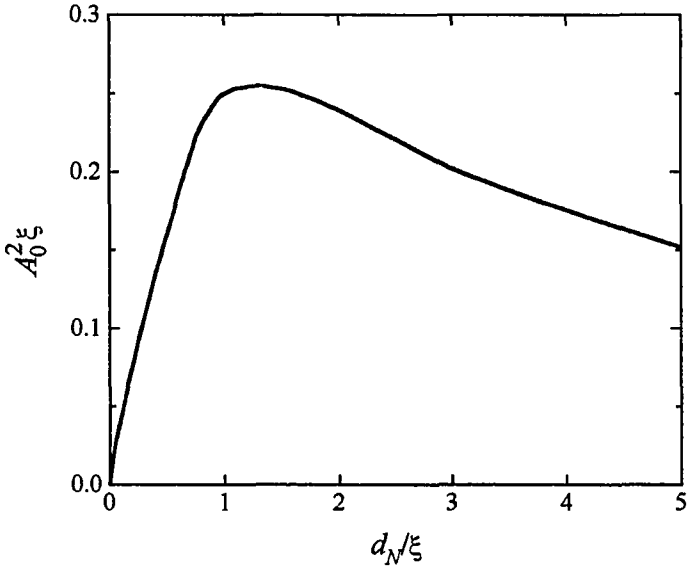

Fig. 4.3 Normalization factor for the lowest bound state A_0^2 shown as a function of d_N.

the thickness of N increases, the likelihood for finding the state at a particular location inside N decreases. In contrast, the reason $A_0^2 \to 0$ abruptly as $d_N \to 0$ is more subtle and results from remarkable behavior of the state as the dG-SJ model reduces to an isolated superconductor. To meet the requirement of no quasiparticle states within the bulk gap, the bound-state energy must leave the range of $0<\varepsilon_0<\Delta_\infty$ in some way. From Eq. 4.10 we find that as $d_N/\xi \to 0$, the state disappears by merging into the gap edge, $\varepsilon_0 \to \Delta_\infty$, where there is a continuum of delocalized scattering states. In fact as d_N/ξ decreases, the bound state begins to look like a scattering state, as seen from Eqs. 4.6. We find that all bound states penetrate across the NS interface into the superconductor, with the penetration depth given by

$$\kappa_n^{-1} = \pi\xi \frac{\Delta_\infty}{\sqrt{\Delta_\infty^2 - \varepsilon_n^2}}. \qquad 4.16$$

Low-lying states, $d_N/\xi >> 1$, $\varepsilon_n << \Delta_\infty$, are clearly localized to the normal metal, as the penetration depth is only $\kappa_n^{-1} \approx \pi\xi$ (see Figure 4.2(a)). However as $d_N/\xi \to 0$ and our last bound state merges into the gap edge, Eq. 4.16 indicates that κ_0^{-1} tends to infinity. In other words, there would be an equal likelihood of finding the state anywhere inside the semi-infinite NS system; this follows the behavior of scattering states beyond the gap edge. Of course, the probability of finding it inside the normal layer then becomes vanishingly small.

The situation is shown quantitatively in Figure 4.4 which contrasts the normalized $|u_0(z)|^2$ for two values of d_N/ξ: 1.0 and 0.1. The wavefunction of the $d_N/\xi=1.0$ state (for which $\varepsilon_0=0.857\Delta_\infty$) attenuates significantly inside S on the scale of ξ. In contrast, the wavefunction of the $d_N/\xi=0.1$ state ($\varepsilon_0=0.998\Delta_\infty$) is nearly constant, behaving much like a delocalized scattering state. Although the energies for the two states only differ by about 14%, CSTM should be able to easily distinguish them from the magnitudes of the

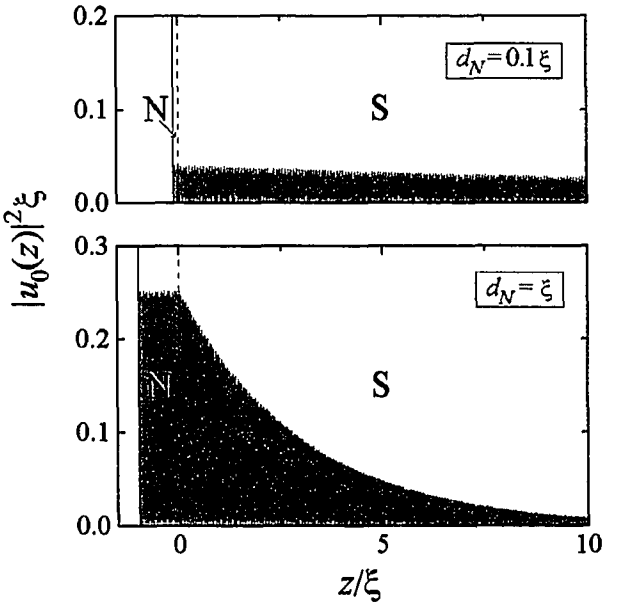

Fig. 4.4 The dG-SJ $|u_0(z)|^2$ for two values of d_N/ξ: 1.0 and 0.1. Only variations in the amplitude can be discerned as in Fig. 4.2(a). We see that the state is much more localized in the d_N/ξ=1.0 case.

respective bound-state peaks in $N(E)$, which are proportional to the amplitude of $|u_0(z)|^2$ inside N. We see that the d_N/ξ=1.0 peak would have a magnitude about 500% greater than the d_N/ξ=0.1 peak. More generally, any d_N in the range of $0<d_N/\xi<1$ could be accurately determined by CSTM by comparing the relative magnitude of the bound-state peak to the d_N-dependence of A_0^2 shown in Figure 4.3. So if the normal metal thickness were not constant but rather a function of location on the sample surface, this approach would offer a sensitive probe of the local $d_N(x,y)$.

4.2.3 Density of states beyond the bulk gap

Unfortunately, our present method becomes computationally-lengthy when applied to eigenstates above Δ_∞. To see the behavior at arbitrary energy $E<<E_F$, we turn to calculations of $N(E)$ based on Green function techniques.[31] Figure 4.5 shows two surface plots of the density of states inside the N layer for the dG-SJ model, as a function of both E and d_N/ξ. Figure 4.5 (top) illustrates that as d_N increases, more states enter into the bulk gap and the magnitudes of all the bound-state peaks decrease. Eventually, the peaks will sufficiently overlap so that individual ones are not discernible. The density of states will then look like a constant function of E, consistent with an isolated normal metal. Figure 4.5 (top) also shows the presence of small $N(E)$ peaks outside the bulk gap. These peaks, known as Rowell-McMillan oscillations, smoothly move to the inside of the gap to become the bound states as d_N increases. Not surprisingly, Rowell-McMillan oscillations are closely related to the bound states, arising from over-the-barrier Andreev reflection.[35]

To see explicitly the manner in which the first bound state enters the bulk gap, Figure 4.5 (bottom) shows an enlargement of the region $0<d_N/\xi<1$. As discussed in Sec. 4.2.2, the magnitude of the bound state increases abruptly as d_N increases from zero. The surface plot shows that the bound-state peak smoothly emerges from the peak at the BCS

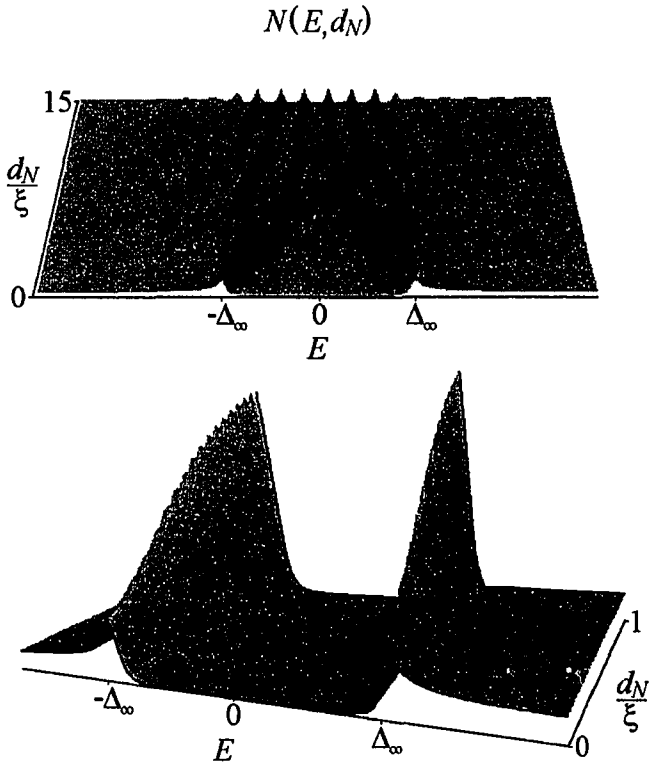

Fig. 4.5 $N(E,d_N)$ for the dG-SJ model calculated from an expression valid for all $E<<E_F$, based on Green function techniques.[31] The top surface plot corresponds to $-3\Delta_\infty<E<3\Delta_\infty$, $0<d_N/\xi<15$. At bottom an enlargement of the region $-2\Delta_\infty<E<2\Delta_\infty$, $0<d_N/\xi<1$ is shown.

gap edge, highlighted in black. Moreover, we see that the increase in the bound-state magnitude inside the gap occurs at the expense of the BCS enhancement in $N(E)$ for energies just beyond the gap. In this way, the character of the density of states changes significantly with the presence of a single quasiparticle bound state.

5. OVERVIEW OF Au-$NbSe_2$ MEASUREMENTS

Prior to this work, the only successful CSTM measurements of spatially-varying superconductivity probed the quasiparticle bound states in magnetic vortices, as discussed in Chapter 1. Instead, it would be compelling to induce spatial variations using normal metal contacts, creating artificially-prepared NS structures. Measuring the bound states in these structures is a more basic experiment, as magnetic flux and screening currents are now decoupled from the problem. The bound-state energies are a function of the pair-potential well, the magnitude of which is determined by the N thickness and the superconducting proximity effect in both N and S. Thus in principle, the proximity effect can be characterized by simultaneously measuring the spectum of bound states and the N thickness. The capabilities of CSTM lend themselves excellently to such a study for structures in which the N and S regions can be identified by topography, such as N islands on a flat S substrate. Our goal was to probe locally the island-substrate geometry to measure the proximity effect at the unprecedented length scales achievable with CSTM.

We selected Au and $NbSe_2$ as the normal metal and superconductor, two chemically inert materials for which a clean, sharp, planar interface can readily be formed.[36] No superconducting transition has been observed in Au down to 3.8×10^{-5}K.[37] $NbSe_2$ is a well-characterized, anisotropic, layered superconductor, which undergoes a superconducting transition at T_c=7.2 K with a bulk energy gap Δ_∞ of about 1.3 meV as discussed in Sec. 3.2. It is similar to the high-T_c superconductors in that the coherence length perpendicular to the layers approaches atomic length scales, $\xi_{S\perp}$=23 Å; parallel to the layers the coherence length is somewhat larger, $\xi_{S\|}$=77 Å.[38] $NbSe_2$ also undergoes a charge-density-wave (CDW) transition at 33 K with a corresponding gap of

Fig. 5.1 A 30 Å x 30 Å topographic image of Au-$NbSe_2$. The periodic corrugations correspond to the atomic lattice of Se atoms on the $NbSe_2$ substrate. We identify the irregular structure as Au, since it appears only after the thermal evaporation.

35 meV. Below 7 K, features of both the CDW and superconducting energy gap are present in the tunneling spectra, as shown in Figure 2.8.

To minimize surface contamination, the samples were prepared *in-situ* using our customized CSTM system. Crystals of $NbSe_2$ (typically 4 mm x 4 mm x 0.2 mm) were freshly cleaved prior to thermal evaporation of Au with nominal thickness of 2 Å to 7 Å, as measured by a crystal monitor. Topographic and spectroscopic measurements were taken with the STM immersed in liquid helium at a temperature of T=1.6 K. We find that the deposited Au forms distinct islands having widths ranging from 40 Å to 150 Å with separations of 20 Å to 100 Å. In the flat regions between islands we observe an atomic lattice consistent with that of clean $NbSe_2$, as shown in Figure 5.1. Spectra were obtained using a chemically-etched Pt-Ir tip, with tunneling resistances ~10^8 Ω. In addition to subtracting background variations due to thermal drift, the CDW gap feature was also removed. This was desirable because the CDW gap results in a distortion of the spectra beyond the superconducting gap, which can interfere with an accurate characterization of the bound states.

5.1 Representative Spectra

Before beginning detailed analyses of the data, we present a brief survey of spectra from different Au islands and discuss them in terms of the dG-SJ model. Figure 5.2 shows four representative spectra: three from islands of various shapes with thicknesses ranging from 10 Å to 140 Å, and one from pure $NbSe_2$. We first observe that the spectra from the less thick islands have a gap-like shape similar to the spectrum of pure $NbSe_2$. That is to say, there is a dip at zero voltage with broad peaks occurring at approximately ±2 mV. However, all of the spectra exhibit an enhancement in the conductance at zero voltage compared to the pure $NbSe_2$ spectrum. This is especially true for measurements from the thickest islands, such as spectrum A from the 140 Å

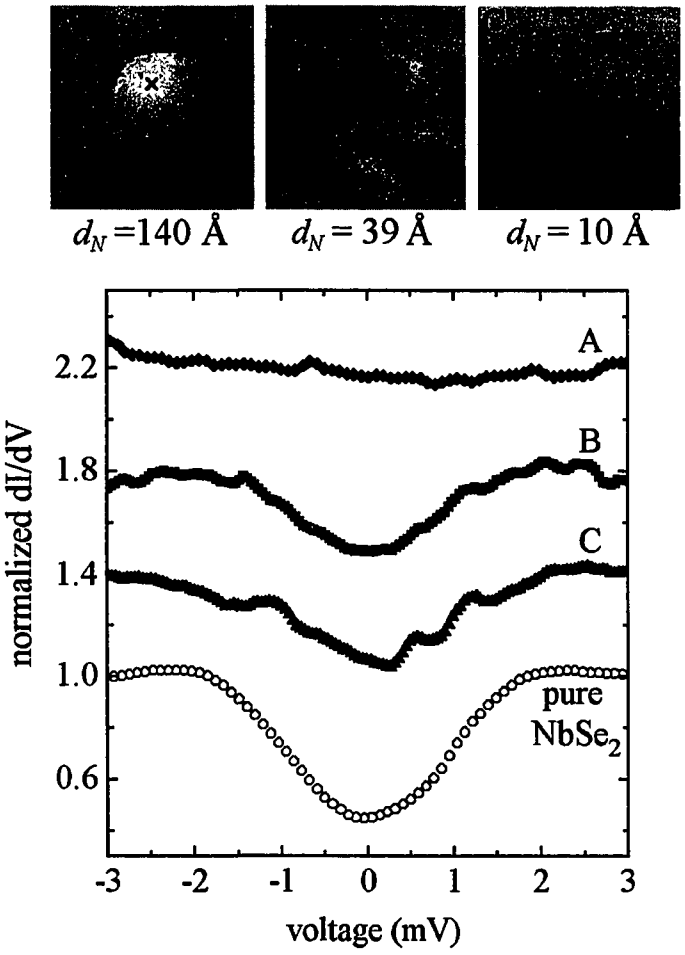

Fig. 5.2 (top) Topographical images of three representative Au islands that have maximum thicknesses ranging from 10 Å to 140 Å as indicated. (bottom) Spectra obtained on the different islands, at the location marked above with an x. Included for comparison at bottom is a representative spectrum of pure $NbSe_2$.

island, for which the zero voltage dip has all but disappeared. There are weak peaks inside the bulk gap, $|V|<1.3$ mV, but they are not robust and are difficult to identify above the background noise. These may be bound-state peaks which are more smeared in energy compared to those of thinner islands, an effect that can result from electronic trajectories parallel to the interface.[30] Although we have been unable to characterize the behavior in detail for Au islands thicker than 70 Å, the position of the peaks appears to be a function of both thickness and the x-y geometry. We conclude generally that the spectra have a less gap-like shape, with a significant density of states well inside the bulk energy gap.

Returning to Figure 5.2, we next consider spectra B and C from islands of thickness 39 Å and 10 Å respectively. The topography of the islands is typical, as those more than 20 Å thick tend to have irregular geometries, while thinner island tend to be more planar. Restricting our attention to only broad features in the spectra (~1mV), we see that the two are very similar, showing peaks near ±2 mV. However, there are significant differences with regard to the fine structure. Spectum C has well-resolved additional peaks occurring within the gap. These reproducible features occur at symmetric voltages with respect to zero, i.e., there are clear peaks at ±1.1 and 0.5 mV, with a less-resolved one at -0.5 mV. In contrast, spectrum B does not clearly show additional peaks. Although there are some hints of additional structure, symmetric features like those of spectrum C cannot be discerned from the background noise. All spectra from islands of thickness between 20 Å and 70 Å are qualitatively similar to B. In these cases, we consider only the broad peaks to be significant.

We can use the dG-SJ model as a starting point to analyze the Au-$NbSe_2$ data. Although the calculation presented in Sec. 4.2 is certainly idealized, neglecting such issues as the proximity effect and the three-dimensional geometry of the islands, it will at least provide a rough idea of the expected behavior. As discussed in Sec. 4.2.1, the length scale for d_N will not be the superconducting coherence length, because Au and

$NbSe_2$ are electronically distinct. Instead it will be set by the $NbSe_2$ energy gap and the Au Fermi velocity, $v_{FN} = 1.40 \times 10^8$ cm/sec,[39] resulting in an effective length scale of $\xi^* = \hbar v_{FN}/\pi\Delta_\infty = 2300$ Å. As this is at least an order of magnitude greater than the thickness of the Au islands in our experiment, we expect to be in the regime $d_N/\xi^* << 1$. From Eq. 4.11, we see that all islands should have exactly one bound state. Therefore the spectra should show just two bound-state peaks, a quasielectron peak above the Fermi energy, and a quasihole peak below. This is consistent with our observations for island thicker than 20 Å if we assume that the broad peaks arise essentially from the bound state. However, the multiple peaks observed for extremely thin islands are clearly beyond the scope of the dG-SJ model, as presented in Sec. 4.2. In fact, these peaks are completely inconsistent with the conventional theory using reasonable values for the effective length scales, even considering the issues of the proximity effect and the three-dimensional geometry of the islands.

In analyzing the data in detail, we first address the spectra of extremely-thin planar Au islands, of thickness less than 20 Å, with the purpose of understanding the origin of the small additional peaks. This analysis also contributes to the study of the proximity effect by indicating the minimum value of Δ in the Au-$NbSe_2$ system. We then turn to our main goal of locally characterizing the proximity effect. To this end, we consider the behavior of the broad spectroscopic peaks near ±2 mV, which are present in all islands of thickness less than 70 Å.

6. SPECTROSCOPY OF EXTREMELY THIN AU ISLANDS

CSTM spectra taken in the vicinity of extremely thin planar Au islands (of thickness less than 20 Å) show behavior which is more complex than predicted by the standard theory: superimposed on the characteristic gap-like spectrum, there are fine structure peaks occurring at symmetric energies with respect to the Fermi energy. Qualitatively, this behavior is observed consistently in all of the several extremely thin islands we have probed. Unfortunately, in many cases it is difficult to characterize the features in detail due to relatively high levels of background noise. We observe generally that the energies and amplitudes of the peaks appear to be a function of the thickness and geometry of a particular island. In this chapter we focus on measurements in which the additional peaks were especially well-resolved. To this end, we consider spectra taken on and near two Au islands of thickness 10 Å and 6 Å. The structure will be discussed in light of recent work by Im, Jagla, and Balseiro, who postulate that it may arise from a single bound state that is split into multiple peaks due to effects of the small number of individual atomic layers in the normal metal.[40]

6.1 Spectroscopic Measurements

Figure 6.1 shows two spectra taken in the vicinity of an island of thickness 10 Å. As indicated in (b), the location of spectum A is clearly on the Au, 20 Å from the nearest edge. In contrast, spectum B which is located just 30 Å away, corresponds to tunneling directly into the $NbSe_2$. Figure 6.1(c) shows the two measurements with a representative spectrum of pure $NbSe_2$ included as a reference. We first note that the general shapes of the two spectra are quite similar, with significant enhancement in the zero-voltage conductance compared to pure $NbSe_2$. In fact, |A-B| does not exceed 0.10 in normalized

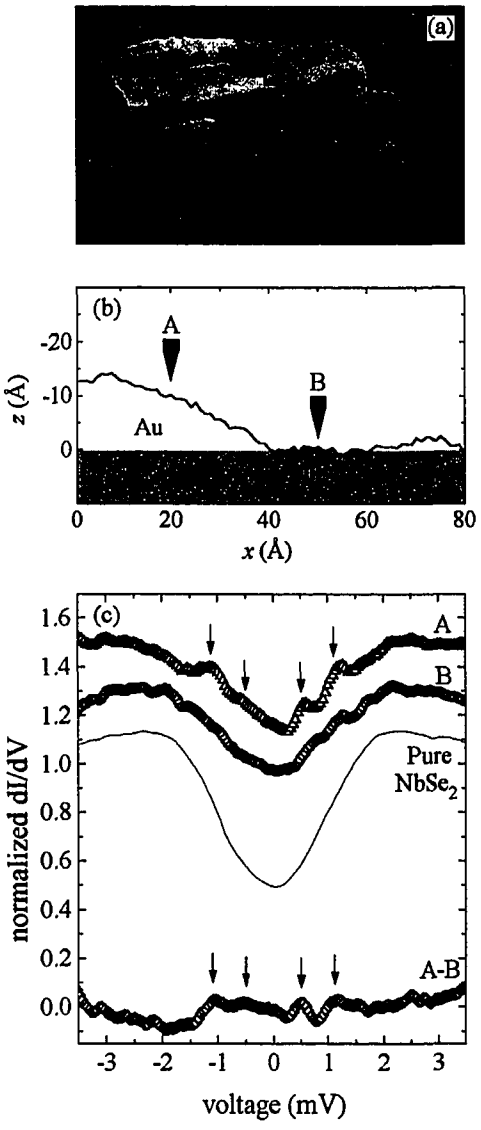

Fig. 6.1 (a) A 100 Å x 100 Å topographic image of a very thin Au island. (b) A cross section of the island taken in the center region of (a), with the x direction perpendicular to the island's edge. (c) Two spectra obtained from the indicated locations. A representative spectrum of pure $NbSe_2$ is included for comparison. Successive curves are shifted upward for clarity.

units. It may seem surprising that spectrum B does not follow the pure-$NbSe_2$ spectrum more closely. This consistently-observed behavior is very significant for spatially characterizing the proximity effect, and will be examined in detail in Chapter 7. Despite their similarities, A and B show significant differences with respect to fine structure features less than 1 mV in width: the small peaks in A at ±1.1 mV and ±0.5 mV, as indicated by the arrows, are either greatly reduced or missing altogether at the corresponding voltages in B. Thus these peaks are likely attributable to the Au film. To highlight this behavior, the difference of the two spectra, A-B, is plotted at the bottom of Figure 6.1(c).

Although the energies of the small peaks vary from island to island, they occur at identical energies in spectra sampling the same island. This is demonstrated for the 6 Å thick island shown in Figure 6.2(a). Figure 6.2(c) shows a series of five spectra taken on the Au at the indicated locations. Once again, on a broad energy scale the spectra generally exhibit enhancement at zero-voltage compared to pure $NbSe_2$ (solid curves). With regard to the fine structure, each of the spectra have conductance peaks at ±0.80 mV discernible above the background noise. The fact that this feature persists at various locations, even along the sloped edge of the island, affirms the robust nature of the fine structure. To isolate the bound state contribution to the spectra, we subtract from each curve the spectum of pure $NbSe_2$, which can be regarded as an approximation for the scattering state contribution. Figure 6.2(d) shows the resulting curves on the energy scale of the bulk gap. Now the ±0.80 mV peaks are the prominent features of each curve. The curves also show less prominent peaks at ±0.25 mV, with perhaps an additional feature at zero voltage. The amplitudes of the peaks are not symmetric in general. For example, the -0.80 mV peak rises 0.1 normalized units above the background in spectrum B, while the +0.80 mV peak rises only a fraction of that amount. The amplitude of corresponding peaks also vary with position, although it is experimentally difficult to map out these

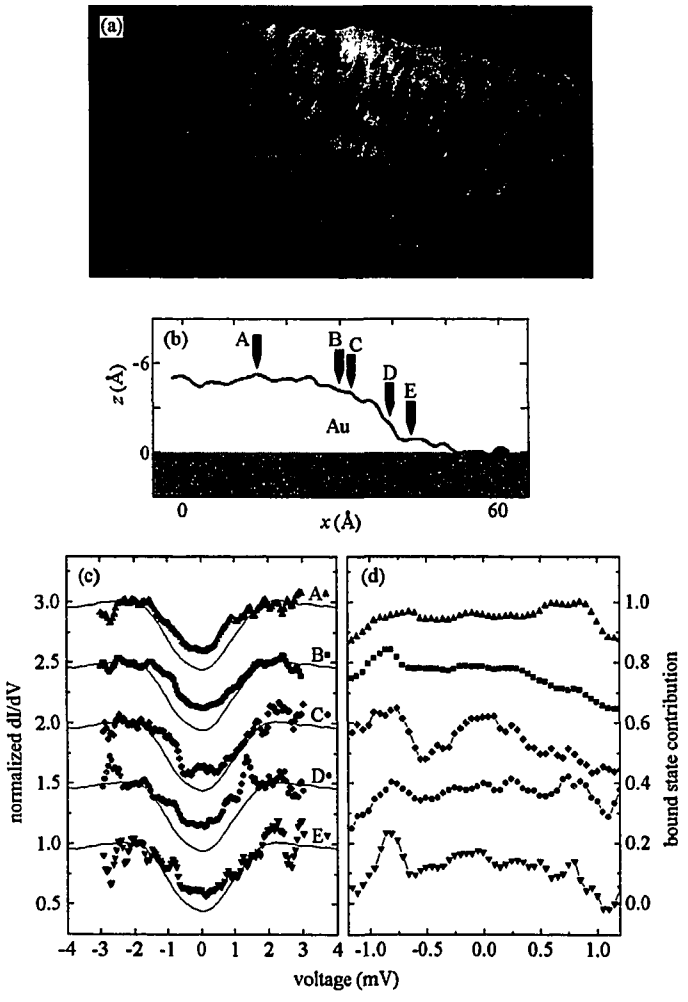

Fig. 6.2 (a) A 250 Å x 250 Å topographic image of a thin, planar Au island. (b) A cross section showing the sloped edge of the island in the center region of (a). (c) A series of five spectra obtained from the indicated locations. Successive curves are shifted upward for clarity. (d) The approximate bound-state contribution to each spectrum, obtained by subtracting the pure $NbSe_2$ spectrum (solid curves in part (c)).

variations. This behavior may reflect oscillations of the bound state wavefunctions in the z direction.[41]

6.2 Im-Jagla-Balseiro (IJB) Model

Our observations of energetically well-defined fine structure peaks localized to the normal metal, are reminiscent of behavior of dG-SJ bound states. However for these extremely thin islands, the spectra should show just two peaks due to a single bound state, as discussed in Chapter 5. In addressing these measurements, H. K. Im, E. A. Jagla, and C. A. Balseiro (IJB) have explored the possibility that a single bound state might produce multiple peaks in the local density of states $N(E,\boldsymbol{r})$.[40] Their insight was based on the three-dimensional nature of the problem. In the dG-SJ model, the fact that quasiparticles can have a component of momentum parallel to the interfaces, $k_{\|}$, leads to a straightforward correction to the calculation presented in Chapter 4 (where only perpendicular trajectories were considered). Quite simply, quasiparticles with more parallel trajectories travel through more normal metal before encountering the interfaces. Because these quasiparticles see a pair-potential well of increased magnitude, including them in calculating $N(E,\boldsymbol{r})$ smoothly broadens the bound-state peak to lower energies.[28,30] But the dG-SJ model assumes a free-electron-gas in the absence of pairing, which may be a poor approximation for an island of atomic dimensions. Perhaps if electronic interactions with the atomic lattice were considered, quasiparticles with parallel trajectories would be found to behave in a more complex manner.

IJB performed calculations which significantly modified the dG-SJ model. Using a tight-binding approximation that takes into account the atomic structure, it was shown that for normal-metal layers approaching atomic thicknesses, a single bound-state results in multiple peaks in $N(E,\boldsymbol{r})$. The additional peaks arise from shifts in the dG-SJ bound-state energy E_0, caused by interactions with the normal-metal lattice. The amount of the

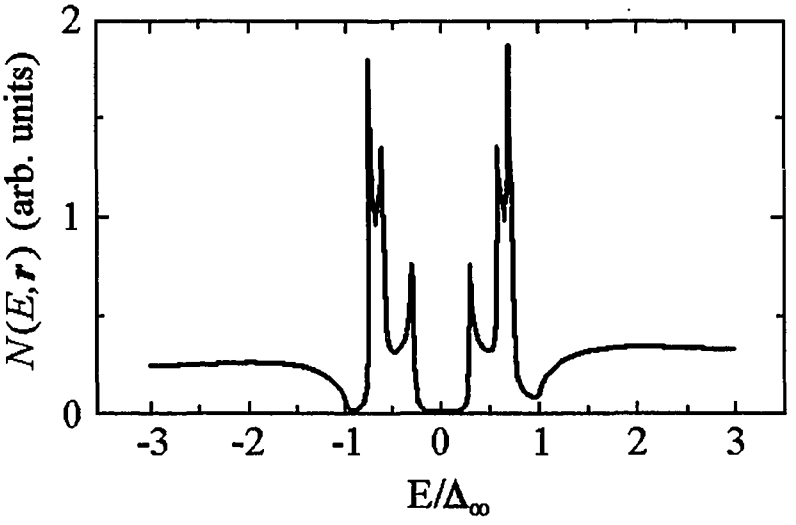

Fig. 6.3 The local density of states inside a Au film 5 atomic layers thick in contact with a bulk crystal of $NbSe_2$, calculated from the IJB model.[40]

shift depends on the particular trajectory, leading to oscillations of E_0 as a function of $k_{\|}$, where the number of minima is on the order of the number of normal-metal atomic layers n_N. Assuming that all trajectories contribute equally to the density of states, all $k_{\|}$ are included in the calculation. The resulting $N(E,\boldsymbol{r})$ has a feature reminiscent of the dG-SJ peak; but there are additional peaks at energies closer to the Fermi level. As n_N increases, the amplitude of the oscillations in $E_0(k_{\|})$ is reduced. Thus, the amplitudes of the additional $N(E,\boldsymbol{r})$ peaks are also reduced, so that the dG-SJ form is retained in the limit $n_N \rightarrow \infty$. Reference 40 explicitly shows this behavior for n_N=30. If the additional peaks are responsible for the fine structure we observe, this behavior would be consistent with the fact that we are unable to resolve them for islands thicker than 20 Å.

Figure 6.3 has been reproduced from reference 40, showing the calculated IJB $N(E,\boldsymbol{r})$ for a Au layer of n_N=5, in contact with a macroscopic $NbSe_2$ crystal. In this case four additional peaks occur at E/Δ_∞ equal to ±0.60 and ±0.26. This is in excellent agreement with the energies of the fine structure peaks observed on the 6 Å island, for which E/Δ_∞ equals ±0.62 and ±0.19 with experimental uncertainties of ±0.10. Unfortunately, it is difficult to compare directly this calculation to our measurements because the exact experimental sensitivity to $k_{\|}$ is unknown; this will affect the amplitudes of the additional peaks. (CSTM spectroscopy is generally more sensitive to parallel trajectories than planar tunnel junctions, but we believe that the perpendicular contribution still dominates.) However, the agreement with respect to peak energies for the 6 Å-island spectra, together with the qualitative agreement with the behavior observed on other islands, represents strong evidence that the additional peaks of the IJB model are indeed the source of the fine structure we observe in Au-$NbSe_2$ spectra.

Having established that a quasiparticle bound state is the most likely source of the fine structure, the data gives significant information with regard to the proximity effect. If the pair potential does not fall off to zero inside the normal metal, having a minimum value of Δ_{min}, the bound state energies must be equal to or greater that Δ_{min}. This has

been shown explicitly for the dG-SJ model,[42] following from the fact that quasiparticles are forbidden at energies below the local $\Delta(\boldsymbol{r})$. Applying this principle to the fine structure peaks, we conclude that Δ_{min} must be equal to or less than the absolute value of the energy of the lowest peak. In the case of the 6 Å island, clear peaks are resolved at ±0.25 mV, indicating that the pair potential inside the Au is at most 0.25 meV. This is a significant reduction compared to 1.3 meV, the value several coherence lengths into the $NbSe_2$. This behavior is contrary to the conventional wisdom which would assume a negligible change in the pair potential for such a thin layer in contact with a bulk superconductor. In the following chapter we use this information toward the main goal of this work: characterizing the complete $\Delta(\boldsymbol{r})$ profile in the Au-$NbSe_2$ system.

7. DIRECT OBSERVATION OF THE PROXIMITY EFFECT IN Au-$NbSe_2$

Spectra taken in the vicinity of different Au islands all show qualitatively similar behavior with respect to the peaks near ±2 mV. In this chapter we analyze in detail representative CSTM measurements taken in the vicinity of a Au island of thickness 39Å. High-quality spectra were obtained which sample several locations from the island summit down to the bare $NbSe_2$ substrate, as indicated in Figure 7.1. This allowed us to probe the proximity effect inside a bulk superconductor at a much smaller length scale than achieved by conventional techniques using tunnel junctions, proximity-effect sandwiches, or point contacts.[43] Surprisingly, we observe a bound state not only in the Au islands, but also when tunneling into the bare $NbSe_2$ surface between islands. This clearly indicates a suppression of the pair potential inside the superconductor near the NS interface. By comparing the data with modeling based on conventional theory, we are able to infer the spatial variation of Δ both perpendicular and parallel to the interface.

7.1 Spectroscopic Measurements

Spectroscopic measurements were taken on the island at 25 Å increments along the path indicated in black in Figure 7.1. A profile of the island is reproduced in Figure 7.2(a), with all the sampled locations indicated. The spectra are shown in Figure 7.2(b), where the curves labeled A through E correspond to sampling from the highest point (A--defined as x=0), down the sloped edge of the island, and finally to the bare $NbSe_2$ surface off the island (D,E). At all locations, we see the gap-like spectrum with a pronounced dip at the Fermi energy and peaks on both sides, as expected from our considerations of the dG-SJ model. Although the local Au thickness varies substantially, the spectra show only small changes with position and, hence, the thickness: there is a variation in the zero-

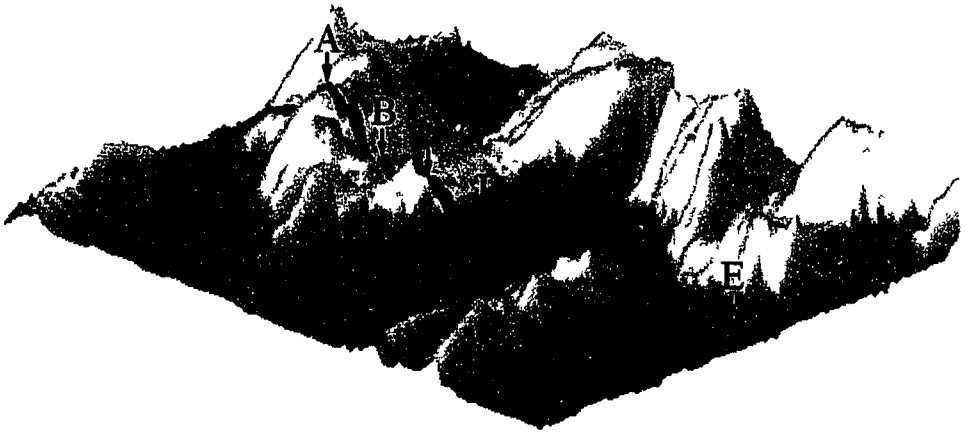

Fig. 7.1 A 250 Å x 200 Å topographic image of the sample surface. The Au island on the left rises 39 Å above the $NbSe_2$ substrate plane. The path along which spectra were taken is indicated in black, with the arrows showing the locations of select spectra.

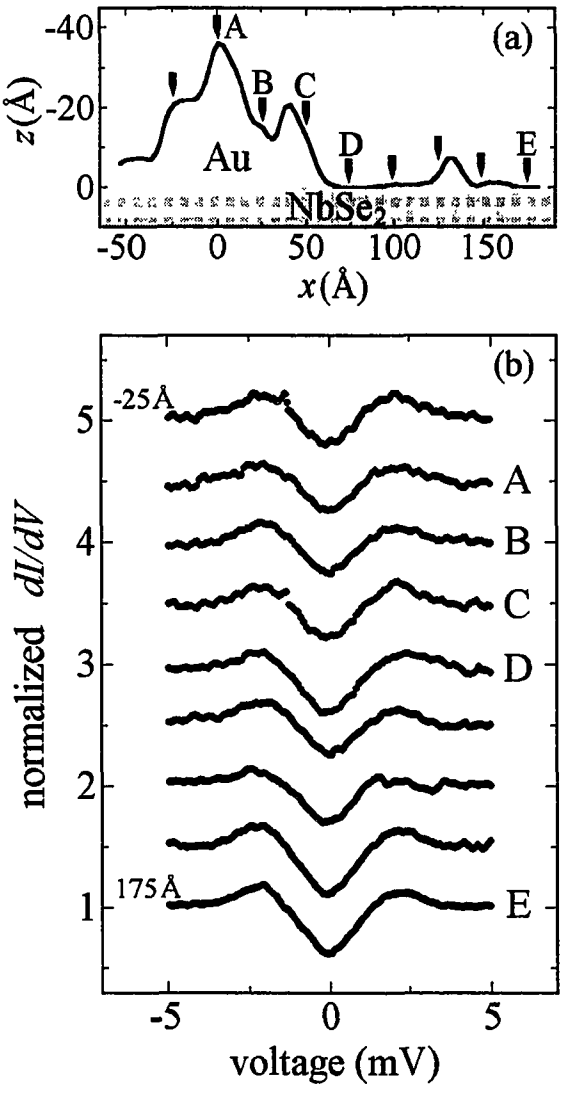

Fig. 7.2 (a) A cross section of the sampled path of the 39 Å island indicating all the sampled location from x=-50 Å to x=175 Å. (b) The measured spectra. The sampled location is increased by an increment of 25 Å for each curve, with successive curves shifted upward for clarity.

voltage conductance of about 10% and a shift in the peak voltage of about 0.2 mV.

To analyze the data, we begin with the usual assumption that the measured spectra represent the convolution of the true density of states with a smearing function. We have found it convenient to describe the smearing by using the Fermi distribution with an elevated effective temperature $T^*>T$, just as for the pure $NbSe_2$ spectra discussed in Sec. 3.2. Alternatively, a phenomenological lifetime broadening term could be used.[25] Although the spectra appear to be similar to the pure $NbSe_2$ spectrum, comparison to the BCS density of states shows that they differ substantially. In the case of pure $NbSe_2$, the spectra can always be well fit with a BCS density of states. This is demonstrated for a representative curve at the bottom of Figure 7.3, with fitting parameters Δ_∞=1.3 meV and T^*=7.6 K. In contrast, we find that for Au-decorated samples, the BCS form (for any choice of Δ_∞ and T^*) cannot adequately fit the tunneling spectra taken either directly on the islands or on the bare $NbSe_2$ surface near the islands. For example, Figure 7.3 shows the unsuccessful fits which result near ±2 mV peaks for spectra A and E, by taking Δ_∞=1.3 meV adjusting T^* until agreement is reached at zero voltage. Alternatively, agreement can be achieved at the conductance peaks only by sacrificing the good fit inside the gap. Basically, the peak feature is too tall and narrow to be consistent with the BCS peak at the gap-edge.

Such poor BCS fits are surprising in light of the expected behavior of bound states in very thin N layers. Because $d_N/\xi^*<<1$ (see Sec. 5.1) there should be only one quasiparticle bound state which is so close to the gap edge that $N(E,\boldsymbol{r})$ is nearly identical to N_{BCS}, as discussed in Secs. 4.2.2 and 4.2.3. We believe the discrepancy arises from the proximity effect of the Au islands which suppresses Δ inside S, creating a significantly larger potential well to support the bound state. The Δ suppression extends even into regions between Au islands because of the nonlocality of the pair-potential.

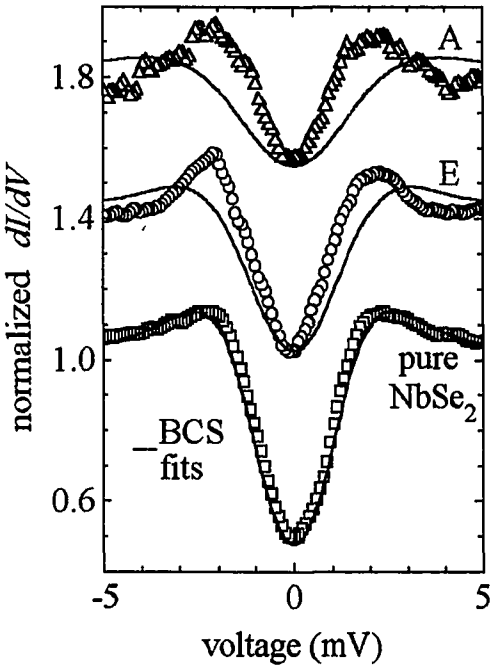

Fig. 7.3 An example attempt to fit spectra A, E, and a representative pure $NbSe_2$ spectrum with the BCS density of states. In this case we take Δ_∞=1.3 meV and adjust T^* until agreement is reached at zero voltage. (The resulting values are 12.7 K, 9.8 K, and 7.6 K respectively.) In general, Au-$NbSe_2$ spectra cannot be adequately fit with any choice of Δ_∞ and T^*.

7.2 Proximity Effect Model

Our basic approach is to determine the spatial profile of Δ in the vicinity of an island by fitting the measured tunneling spectra to solutions of the Bogoliubov-de Gennes equations for a trial profile. In lieu of an involved three-dimensional calculation, we use the following phenomenological model. We assume that the profile of Δ can be parametrized in a quasi-one-dimensional form,

$$\Delta(x,y,z)\big|_{z>0} = \Delta_\infty \tanh\left[\frac{z+z_0(x,y)}{\sqrt{2}\xi_{S\perp}}\right]$$

inside the superconductor, and Δ=0 inside a normal-metal layer of thickness d_N, as shown in Figure 7.4. We use the value of Δ on the S side of the interfacial plane, $\Delta_0(x,y) = \Delta_\infty \tanh[z_0(x,y)/\sqrt{2}\,\xi_{S\perp}]$, as a convenient parameter to characterize the magnitude of the Δ suppression in S. This model follows the conventional behavior for the proximity effect inside S,[22] and is consistent with the observations of low-energy fine-structure peaks in extremely thin Au overlayers. The resulting pair-potential well traverses the NS interface. Consequently, the strength of the well and, hence, the energy of the bound states, depend both on $d_N(x,y)$ and $\Delta_0(x,y)$.

Although it is possible and somewhat illuminating to compute the density of states from the Bogoliubov-de Gennes equations directly,[44] this procedure is computationally-lengthy. Instead, we have developed an efficient Green function algorithm for solving the Gor'kov equations numerically for an arbitrary one-dimensional profile $\Delta(z)$. Although we do not require the self-consistency condition, Eq. 4.2, to be met, the procedure yields a reasonable approximation to the electronic density of states. Our approach is to approximate the smoothly-varying pair-potential by a sequence of step

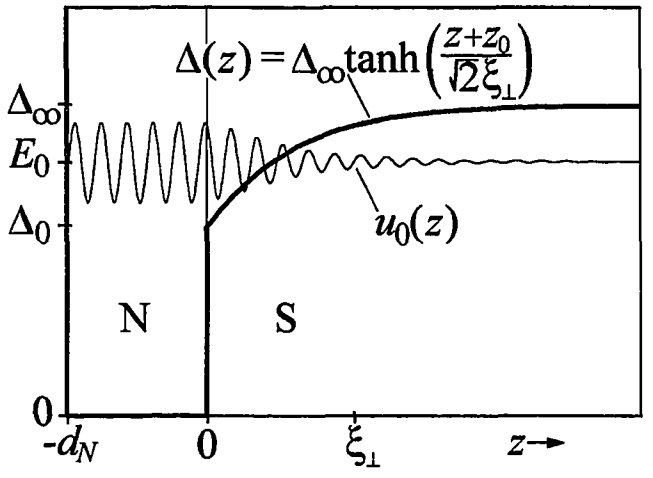

Fig. 7.4 Our proximity-effect model. In addition to the Δ=0 normal layer, the proximity effect induces a region of reduced Δ near the interface. For thin N, the resulting pair-potential well will support exactly one quasiparticle bound state, the wavefunction of which is indicated schematically by the oscillating curve.

functions (typically 50) and then calculate the surface density of states using a technique similar to that developed for a single-step pair-potential.[45] The model includes distinct Fermi velocities v_{FN} and v_{FS} and effective masses m_N and m_S for the N and S layers to account for differences in their electronic structures. The model also includes a δ-function single-particle potential to account for boundary imperfections. This term enhances the probability that a quasiparticle will undergo ordinary reflection rather than Andreev reflection, but we have found it unnecessary to invoke this in the present experiment. The calculated density of states is then thermally-broadened and fit to the experimental tunneling spectra by adjusting only two parameters: Δ_0 and T^*. The effective temperature is allowed to vary with location because local surface structure may contribute to the spectral broadening.

7.3 Proximity Effect Perpendicular to the Interface

We have applied our proximity-effect model to the measured spectra at each sampled location, using the measured topographical height $d_N(x,y)$ above the $NbSe_2$ surface, and the following material parameters for the $NbSe_2$-Au system: Δ_∞=1.3 meV, $\xi_{S\perp}$=23 Å, v_{FS}/v_{FN}=0.01, m_S/m_N=2.76, and E_{FS}/Δ_∞=100.[46,47] The values of Δ_0 and T^* were determined by using a least-squares fit to the spectrum at each location. As shown in Figure 7.5, excellent fits to the measured spectra were obtained. The best fit values for Δ_0/Δ_∞ varied from 0.07-0.38, with T^* nearly uniform in the range 7.9±0.6 K, as indicated in Table 1.

To illustrate the sensitivity of our method to Δ_0, Figure 7.6 compares the best-fit curves to curves obtained with Δ_0=0 (maximum suppression in S) and $\Delta_0=\Delta_\infty$ (no suppression). At the summit of the island, location A (Figure 7.6(a)), we see that the best fit is achieved at a surprisingly low value of $\Delta_0 \cong 0.1\,\Delta_\infty$. In fact, this fit is only a slight improvement over the Δ_0=0 curve. The $\Delta_0=\Delta_\infty$ curve, which corresponds to a pair-

x(Å)	$d_N/\xi_{S\perp}$	Δ_0/Δ_∞	T^*(K)	E_0/Δ_∞
-25	0.91	0.07	7.3	0.888
0	1.57	0.12	7.6	0.892
25	0.65	0.17	7.9	0.909
50	0.51	0.21	7.4	0.920
75	0.00	0.37	8.0	0.950
100	0.03	0.14	8.4	0.904
125	0.10	0.32	9.9	0.944
150	0.03	0.38	7.5	0.952
175	0.00	0.38	7.7	0.952

Table 1 The parameters used to generate the theoretical curves. The first two columns list the topographical coordinates x and $d_N=z(x)$ of each measured spectrum. The next two columns show the values of the two parameters, Δ_0 and T^*, which were adjusted in the theoretical curves to achieve the best fit, followed by the corresponding bound state energy E_0.

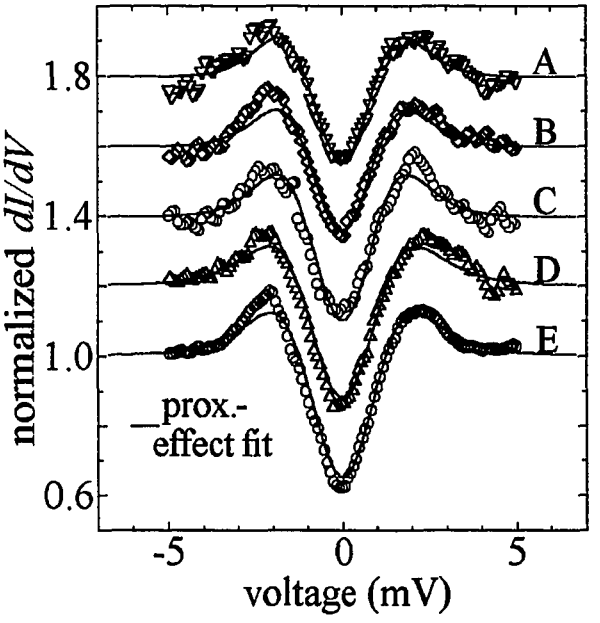

Fig. 7.5 The fit achieved by our proximity-effect model for a series of five of the spectra from the highest point on the Au (A) down to the $NbSe_2$ substrate (D,E) as indicated in Figures 7.1 and 7.2. The fitting parameters are shown in Table 1.

potential well only inside the Au, is clearly inadequate. Even at location E (Figure 7.6(b)) where the tunneling is directly into the bare superconductor, Δ_0 is substantially less than Δ_∞, a definite indication that the pair-potential inside the superconductor is strongly suppressed by proximity to the normal metal island.

The role of the Δ suppression at the interface can be clearly seen by removing the broadening from the calculated conductance curves, which yields the true density of states $N(E)$. This is shown for the curves of Figure 7.6(a,b) in Figure 7.6(c,d). We see that at locations A and E, the best-fit $N(E)$ (solid curves) are dominated by bound state peaks at 0.89 Δ_∞ and 0.95 Δ_∞ respectively. Figure 7.6(d) also highlights why the spectra cannot be adequately fit with the BCS density of states, which is shown by the dashed curve. (This curve corresponds to $\Delta_0=\Delta_\infty$and $d_N=0$, in which case our model reduces to the isolated BCS case.) Although the δ-function-like bound-state peak occurs only at a slightly reduced energy compared to the BCS peak, it has a greatly increased amplitude. In fact, as discussed in Sec. 4.2, the magnitude of the pair potential well influences drastically the amplitude of the peak. This is essentially the reason that our method allows Δ_0 to be determined to a good precision by fitting the measured bound state feature.

Our modeling also predicts that the conductance spectra should have little dependence on the local Au thickness d_N, as we observe and in accord with the expected behavior for very thin N layers.[30] In contrast, the spectra depend strongly on the magnitude of the Δ suppression inside the superconductor, even though this suppression only extends to a depth of $\xi_{S\perp}$, which is comparable to d_N. This occurs because of the large mismatch in Fermi velocities between the Au and $NbSe_2$, for which $v_{FN}/v_{FS}\approx 100$. To get an intuitive picture of this situation, it is helpful to consider the behavior of the waves constructed from the difference of particle and hole wave numbers, introduced in Sec. 4.2.1 while discussing the dG-SJ model. We can still think of the problem in terms of waves which oscillate with a much longer wavelength than the actual wavefunctions,

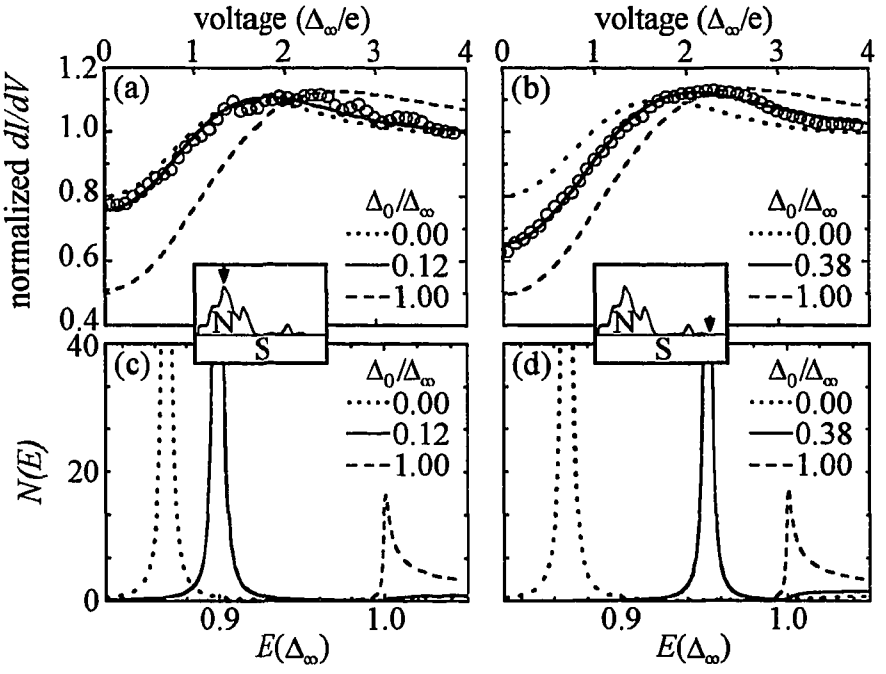

Fig. 7.6 (a,b) Demonstration of the sensitivity of our fitting procedure to Δ_0, with the best fits shown as the solid curves. (c,d) The densities of states extracted from the (a,b) curves. The bound quasiparticle states are clearly seen as the dominant δ-function-like peaks.

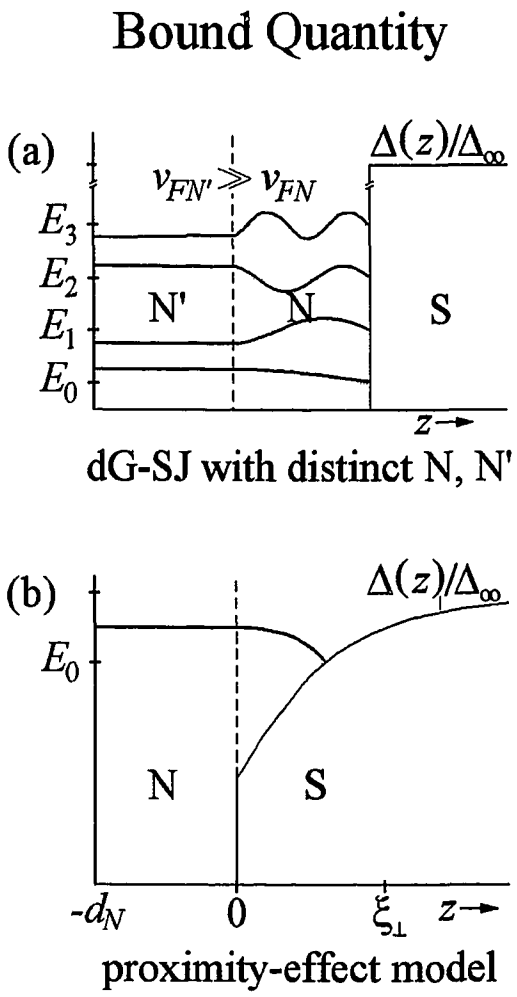

Fig. 7.7 Schematic of the intuitive picture showing the behavior of the bound wave with two effective length scales. (a) The 4 lowest-energy waves for the dG-SJ model with a normal-metal layer N' in addition to the usual N. If $v_{FN'} >> v_{FN}$, we must allow the waves to oscillate with a much longer wavelength in N'. (b) Due to the different electronic parameters of Au and $NbSe_2$, an analogous situation occurs for our proximity effect model in which the pair potential well traverses the NS interface.

qualitatively following the behavior of conventional bound states. However in the presence of a Fermi velocity mismatch, the oscillations must be considered to have distinct wavelengths in each material, as illustrated in Figure 7.7. In our present model, we can consider our bound wave to have two effective length scales: in the normal it is of order $\hbar v_{FN}/\pi\Delta_\infty >> d_N$, whereas in the superconductor it will be of order $\hbar v_{FS}/\pi(\Delta_\infty - \Delta_0) \sim \xi_S$. The resulting wave winds much more slowly in N than in S, so that the bound state energy is mostly determined by the magnitude of the well in S. It should once again be emphasized that we only construct these wave as a guide for our intuition; the physically significant quantities are the wavefunctions u_n and v_n.

7.4 Proximity Effect Parallel to the Interface

We now examine the spatial dependence of the pair-potential in lateral directions. The behavior shown in Figure 7.8 is qualitatively consistent with measurements in all probed regions: the minimum Δ_0 (maximum Δ suppression in S) occurs directly beneath the islands and the maximum Δ_0 (or minimum suppression) occurs in the regions between islands. (As topographic data suggests dual tunneling sites at location x=100 Å, an effect encountered frequently when probing irregular structures by STM, we exclude this point.) For the case of an isolated Au island, the pair-potential is expected to recover to the pure $NbSe_2$ limit of $\Delta_0=\Delta_\infty$ beyond the some characteristic length scale L. Since L essentially measures the range of the proximity effect in the lateral direction, we expect it to be of order $\xi_{S||}$ (77 Å). Unfortunately, the thermal evaporation method of sample preparation yields Au islands of a variety of shapes and sizes with no control of their relative positions. The resulting lack of sufficient separation prevents us from directly observing the isolated-island limit.

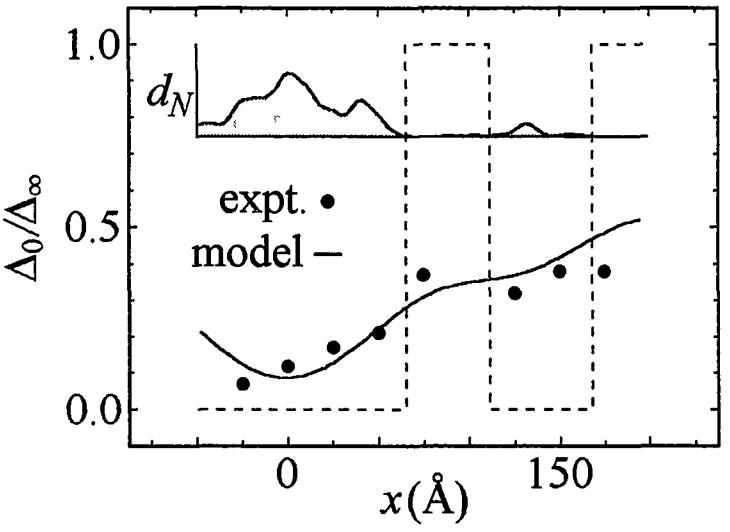

Fig. 7.8 Lateral dependence of interfacial pair potential Δ_0. The experimental values (dots) are compared to a simple model (solid curve) based on the Au topography. The dashed step function shows a cross section of the boundary-value based function $\Delta_0^{\text{disc}}(x,y)$, which is determined by the topography shown in the inset. $\Delta_0^{\text{disc}}(x,y)$ is then broadened in two dimensions in order to estimate the characteristic length scale L.

To deduce L approximately from our data, we use the following model for $\Delta_0(x,y)$. Because in the absence of lateral coherence Δ would only be suppressed directly beneath the Au islands, we construct a simple function $\Delta_0^{\text{disc}}(x,y)$ which has the value Δ_0^{min} in regions covered with Au, but equals the full bulk gap Δ_∞ elsewhere; a profile of the resulting discontinuous function is shown dashed in Figure 7.8. The lateral proximity-effect is then accounted for by broadening $\Delta_0^{\text{disc}}(x,y)$ by convolution in two dimensions with a Gaussian distribution of width L,

$$\Delta_0(\vec{\rho}\,) = \frac{2}{L^2\pi}\int \Delta_0^{\text{disc}}(\vec{r})\, e^{-2(\vec{\rho}-\vec{r})^2/L^2}\, d\vec{r}\ ,$$

where $\vec{\rho} = x\hat{x} + y\hat{y}$ in the interfacial plane.

We apply this model to calculate $\Delta_0(x)$ along the trajectory of Figure 7.1. With the topography dictating the locations of the islands, only Δ_0^{min} and L are free parameters, determined by a least-squares fit to the data. We see that the results of the model, the solid curve in Figure 7.8, is a reasonable fit to the measured values of $\Delta_0(x)$. The best-fit value for L is 81 Å=1.05 $\xi_{S||}$, in excellent agreement with the accepted coherence length parallel to the layers that is expected to set the lateral length scale. The best-fit Δ_0^{min} is $0.00\Delta_\infty$, which indicates that a complete suppression of the pair-potential would occur entirely inside the superconductor for a $NbSe_2$ crystal with a thin, continuous Au over-layer.

7.5 Discussion

In light of our examination of Δ_0 in both the perpendicular and parallel directions, we conclude that the pair-potential is almost completely suppressed inside the $NbSe_2$. This is in sharp contrast to the standard picture of the proximity effect. In this view, the

value of Δ on the S side of an NS interface is expected to be suppressed to $\Delta_0 \approx \Delta_\infty[1-\xi_S/(\xi_S+\xi_N)]$, with even less suppression occurring for thin normal-metal layers, $d_N<\xi_N$. As $\xi_{S\perp}$=23 Å and ξ_N~1μm for our system, a suppression of no more than a few percent would be expected. In a detailed, self-consistent calculation following the conventional theory, specifically addressing the Au-$NbSe_2$ system,[48] a drop in Δ of 20-30% inside the $NbSe_2$ is found, significant but still considerably less than we observe.

The mechanism for the severe suppression of the pair potential at the interface is not known. However, a plausible explanation for this effect follows from the fact that for our superconductor ξ_S does not exceed greatly k_F^{-1}. In fact, perpendicular to the layers, $k_F^{-1}\cong$33 Å so that $k_F\xi_S\cong$0.7.[46] In the conventional picture,[27] it is always assumed that the effective interaction parameter g drops abruptly from its bulk value in S to a lower value in N over a length ξ_g which is much shorter than ξ_S. This leads to a profile for the pair potential which has two distinct regions: (1) a suppression of Δ over the length ξ_S due to the leaking of the Cooper pairs out of the superconductor, i.e., via the conventional proximity effect, and (2) a sharp drop to zero at the interface reflecting the profile of g. This behavior is shown in Figure 4.1. However, because $\xi_g \sim k_F^{-1}$ this view is applicable only when $k_F\xi_S>>1$, as discussed in Sec. 4.1. In the Au-$NbSe_2$ system, $\xi_S \sim \xi_g$ so that the clear separation of these regions cannot be made. Therefore, we believe that the profile of Δ that we extract from our data combines both the conventional proximity suppression of Δ and its modulation by the profile of g. This represents the first observation of spatial structure of the interaction parameter.

Although no detailed calculations of this phenomenon have been performed, qualitatively, it is clear that an enhanced suppression of Δ can occur inside S if $\xi_S \sim \xi_g$, as shown schematically in Figure 7.9. It should be stressed that as we believe the behavior to be beyond the standard theory, the tanh-shaped Δ profile of our model is only an approximation. The actual profile is probably more reminiscent of the one sketched in Figure 7.9. With regard to our modeling, the measured spectra are fit by selecting an

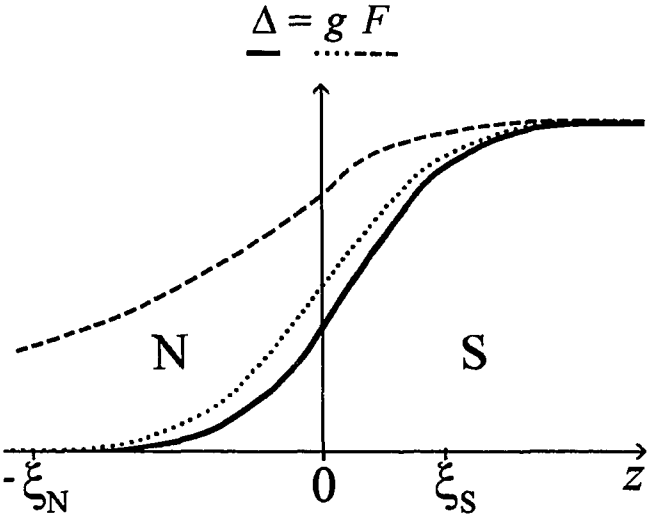

Fig. 7.9 Schematic view of the proximity effect under the condition $\xi_S \sim \xi_g$. Compared to the conventional picture shown in Figure 4.1, the pair potential can undergo a greater reduction (relative to ξ_S) inside S.

interfacial value Δ_0 significantly lower than the prediction of the standard theory. In this way, the model pair-potential well can assume the magnitude necessary to support the observed bound state. In other words, if we consider the areas of the respective pair-potential wells, $\int(\Delta_\infty - \Delta(z))dz$, the true $\Delta(z)$ profile will give approximately the same value as the model $\Delta(z)$. Taking Δ_0=0, this works out to be 3.0 x 10^{-2} eV-Å for the Au-$NbSe_2$ system. Generally speaking, behavior similar to Au-$NbSe_2$ should occur for all NS interfaces with short coherence length superconductors. The enhanced Δ suppression should be particularly pronounced for the high-T_c cuprates, having coherence lengths as short as ~3 Å.

8. SUMMARY AND FUTURE DIRECTIONS

In summary, we have performed local spectroscopic measurements across NS interfaces with CSTM by probing small Au islands in contact with a large superconducting $NbSe_2$ crystal. On the extremely thin islands, we observe multiple-peaked densities of states which we believe arise from the interactions of a single bound state with the normal-metal lattice of ions. In the case of an island of thickness 6 Å, clear peaks are resolved as low as ±0.25 mV. This indicates that the pair potential falls off from the value of 1.3 meV several coherence lengths into the $NbSe_2$, to at most 0.25 meV inside the Au. This behavior is contrary to the conventional wisdom which would assume a negligible change in the pair potential for such a thin layer in contact with a bulk superconductor.

We characterize further the behavior of the pair potential by resolving the densities of states at various locations both on and near thicker islands. A quasiparticle bound state is observed even when tunneling directly into the $NbSe_2$ between islands. This is clear evidence for a significant reduction of the pair potential inside the $NbSe_2$ due to the proximity of the normal Au. By invoking a proximity effect model, we are able to characterize the vertical and lateral variation of the pair-potential inside the superconductor. We believe that the severe suppression, which is inconsistent with the standard picture of the proximity effect, may arise from the short coherence length of the superconductor, so that the spatial variation of the interaction parameter becomes important.

We have demonstrated the potential of CSTM measurements to elucidate the electronic structure of nanoscale superconducting systems. We hope to continue this work at a steady pace, although we find the measurements to be difficult to perform due to the extreme vibrational sensitivities, and the high degree of mechanical stability

demanded of the tip and sample. Surface cleanliness will also continue to be an issue as many of the planned experiments rely on electron-beam lithography to control the geometry of fabricated structures. While this capability can significantly improve our capacity to characterize spatially NS systems, it also involves exposing the samples to a variety of environments during the different processing stages. We find that extra care must be taken to minimize the resulting contamination in order to perform spectroscopic measurements.

Future plans include experiments which will test and/or build upon the conclusions of this work. For example, the goal of a current effort is to resolve the density of states between adjacent Au islands on a Nb substrate. As the islands are fabricated with electron-beam lithography, their separation can now be varied over at least an order of magnitude, up to the 1 μ scale. This will allow the lateral extent of the proximity effect to be measured in detail, as opposed to the estimate performed in this work. With regard to the proximity effect perpendicular to the interface, we hope to repeat these measurements using a variety of superconductors with different coherence lengths. By measuring the pair-potential suppression in S as a function of ξ_S, we can test our belief that the large suppression found in the Au-$NbSe_2$ system arises strictly due to the fact that $\xi_S \sim \xi_g$.

Another series of experiments will search for bound state structure due to lateral confinement inside superconducting layers of thickness less than ξ_S, induced by the proximity effect. For example, the electronic environment beneath a disk-shaped island of radius less than ξ_S should be similar to that of a magnetic vortex, i.e., there will be a cylindrical pair-potential well. Considerable insight could be gained by comparing the behavior of the bound states in such a system to the bound states of a vortex. Another instructive normal-metal geometry is a simple line. If the width of the line were less than ξ_S while the length were much greater than ξ_S, the confinement inside S would be effectively in one direction. Hence, the bound-state behavior could be tested against the

predictions of relatively simple modeling, similar to the dG-SJ model presented in Chapter 4. In this case, oscillations of the bound wavefunctions along the confinement direction may be resolved more directly than in the Au-$NbSe_2$ samples of this work.

Of course there are possible extensions of this work to many related systems. In particular, we would like to attempt to probe NS geometries which incorporate high-T_c superconductors and semiconductor heterostructures. With respect to the high-T_c superconductors, the spatial structure of laterally confined bound states should reflect the symmetry of the order parameter, a key issue in the current theories of these materials. With regard to semiconductor heterostructures, fabricating systems in which these materials electrically contact one or more superconductors, such as Nb, allows for the possibility to observe the bound-state behavior in highly ideal environments, where the dimensionality and electronic parameters of the normal region can be controlled.

REFERENCES

1. G. Binnig, H. Rohrer, Ch. Gerber, and E. Weibel, Physica **109** and **110B**, 2075 (1982); Appl. Phys. Lett. **40**, 178 (1982); G. Binnig and H. Rohrer, Helv. Phys. Acta **55**, 726 (1982).]

2. I. Giaever, Phys. Rev. Lett. **5**, 147 (1960); Phys. Rev. Lett. **5**, 464 (1960).

3. G. Binnig, H. Rohrer, Ch. Gerber, and E. Weibel, PRL 50, 120 (1983).

4. H. F. Hess, R. B. Robinson, R. C. Dynes, J. M. Valles, Jr., and J. V. Waszczak, Phys. Rev. Lett. **62**, 214 (1989); H. F. Hess, R. B. Robinson, and J. V. Waszczak, Phys. Rev. Lett. **64**, 2711 (1990).

5. J. D. Shore, M. Huang, A. T. Dorsey, and J. P. Sethna, Phys. Rev. Lett. **62**, 3089 (1989).

6. Ch. Renner, *Low Temperature Scanning Tunneling Microscopy and Spectroscopy of Layered Superconductors*, Ph.D. dissertation, Département de Physique de la Matière Condensée, Université de Genève, 1993.

7. S. Park and R. C. Barrett, in *Methods of Experimental Physics, Vol. 27, Scanning Tunneling Microscopy*, edited by J. A. Stroscio and W. J. Kaiser (Academic Press, Boston, 1993), pp. 60-64.

8. E. Stoll, A. Baratoff, A. Selloni, and P. Carnevali, J. Phys. C: Solid State Phys. **17**, 3073 (1984).

9. M. Tinkham, *Introduction to Superconductivity* (Krieger, Malabar, Florida, 1980).

10. T. Chen, S. H. Tessmer, J. R. Tucker, J. W. Lyding, and D. J. Van Harlingen, J. Vac. Sci. Technol. B **9**, 1000 (1991).

11. J. Tersoff and N. D. Lang, in *Methods of Experimental Physics, Vol. 27, Scanning Tunneling Microscopy*, edited by J. A. Stroscio and W. J. Kaiser (Academic Press, Boston, 1993), pp. 24-27.

12. In addition to our own experience this phenomenon has been reported by M. A. Dubson and J. Hwang, Rev. Sci. Instrum. **63**, 3643 (1992).

13. S. H. Tessmer, D. J. Van Harlingen, and J. W. Lyding, Rev. Sci. Instrum. **65**, 2855 (1994).

14. A scanning head design could be based on a vertical inertial walker such as the one developed by Ch. Renner *et al*: Ch. Renner, Ph. Niedermann, A. D. Kent, and Ø. Fischer, Rev. Sci. Instrum. **61**, 965 (1990).

15. For an introduction to UHV sample preparation techniques and a brief overview of UHV STM see H. Lüth, *Surfaces and Interfaces of Solids* (Springer, Berlin, 1993).

16. Purchased from Janis Research Co., 2 Jewel Drive, Wilmington, Mass. 01887, (508) 657-8750.

17. Sonex acoustical sheets (NX-3) purchased from Illbruck Inc., Sonex Div., 3800 Washington Ave. N, Minneapolis, MN 55412, (800) 662-0032.

18. Ithaco model #564 purchased from Ithaco Inc., 735 W. Clinton St., Box 6437, Ithaca, NY 14851, (607) 272-7640.

19. RHK model STM 100 purchased from RHK Technology Inc., 1750 W. Hamlin Road, Rochester Hills, MI 48309, (313) 656-3116.

20. J. W. Lyding, S. Scala, J. S. Hubacek, R. Brockenbrough, and G. Gammie, Rev. Sci. Instrum. **59**, 1897 (1988); G. Gammie, *Scanning Tunneling Microscopy of Quasi-One-Dimensional Charge-Density Wave Materials*, Ph.D. dissertation, Department of Electrical and Computer Engineering, University of Illinois at Urbana-Champaign, 1991.

21. J. Bardeen, L. N. Cooper, and J. R. Schrieffer, Phys Rev. **108**, 1175 (1957).

22. P. G. de Gennes, *Superconductivity of Metal and Alloys* (Benjamin, New York, 1966).

23. E. Rovolinsky, B. E. Brown, D. J. Beerntsen, and C. H. Armitage, J. Less-Common Met. 8, 63 (1965).

24. H. F. Hess, in *Methods of Experimental Physics, Vol. 27, Scanning Tunneling Microscopy*, edited by J. Stroscio and W. Kaiser (Academic Press, Boston, 1993), pp. 432-434.

25. R. C. Dynes, V. Narayanamurti, and J. P. Garno, Phys. Rev. Lett. **41**, 1509 (1978).

26. T. P. Orlando and K. A. Delin, *Foundations of Applied Superconductivity* (Addison-Wesley, New York, 1991), Table F.2.

27. G. Deutscher and P. G. de Gennes in *Superconductivity*, ed. by R. D. Parks (Dekker, NY, 1969).

28. P. G. de Gennes and D. Saint-James, Phys. Lett. **4**, 151 (1963); for more algebraic details see W. N. Mathews, Jr., *The Bogoliubov Equations and their Application to a Normal-Superconductoing Boundary*, Ph.D. dissertation, Department of Physics, University of Illinois at Urbana-Champaign, 1966.

29. D. Bellanger, J. Klein, A. Leger, M. Belin, and D. Defourneau, Phys. Lett. **42A**, 459 (1973); J. M. Rowell, Phys. Rev. Lett. **30**, 167 (1973).

30. G. B. Arnold, Phys. Rev. B **18**, 1076 (1978).

31. W. J. Gallagher, Phys. Rev. B **22**, 1233 (1979).

32. E. L. Wolf, *Principles of Electron Tunneling Spectroscopy* (Oxford, New York, 1989).

33. A. F. Andreev, Zh. Eksp. Teor. Fiz. **46**, 1823 (1964) [Sov. Phys. JETP **19**, 1228 (1964)].

34. S. Gasiorowicz, *Quantum Physics* (John Wiley & Sons, New York, 1974), pp. 75-86.

35. J. M. Rowell and W. L. McMillan, Phys. Rev. Lett. **16**, 453 (1966).

36. Secondary Ion Mass Spectroscopy measurement of Au-NbSe2 are consistent with minimal interfacial diffusion.

37. Ch. Buchal *et al.*, Solid State Commun. **42**, 43 (1982).

38. P. de Trey, S. Gygax, and J. P. Jan, J. Low Temp. Phys. **11**, 421 (1973).

39. N. W. Ashcroft and N. D. Mermin, *Solid State Physics* (Saunders, Philadelphia, 1976), Table 2.1.

40. H. K. Im, E. A. Jagla, and C. A. Balseiro, Phys. Rev. B **50**, 10117 (1994).

41. S. H. Tessmer, D. J. Van Harlingen, and J. W. Lyding, Phys. Rev. Lett. **70**, 3135 (1993).

42. D. Saint-James, J. Physique **25**, 899 (1964).

43. P. C. van Son, H. van Kempen, and P. Wyder, Phys. Rev. Lett. **59**, 2226 (1987).

44. F. Gygi and M. Schluter, Phys. Rev. B **41**, 822 (1990).

45. T. Wolfram, Phys. Rev. **170**, 481 (1968).

46. J. Graebner, M. Robbins, Phys. Rev. Lett. **36,** 422 (1976).

47. W. Y. Liang, J. Phys. C **6**, 551 (1973).

48. B. Stojkovic and O. Valls, Phys. Rev. B **50**, 3374 (1994).

VITA

Stuart Holden Tessmer was born in Seattle, Washington on June 1st, 1966. As an undergraduate, he attended the University of Washington where he received the Undergraduate Merit Scholarship in 1985, and graduated in 1989 with a B.S. Cum Laude in Physics. As a graduate student, he has attended the University of Illinois since 1989. He was awarded the Physics Department Summer Fellowship in 1989, the GAANN Fellowship in Physics in 1994, and received an M.S. in Physics in 1992. He was named as an NSF Graduate Fellowship Honorable Mention in 1990.